

Propagation of Slow Slip Events on Rough Faults: Clustering, Back Propagation, and Re-rupturing

Yudong Sun¹ and Camilla Cattania²

¹Massachusetts Institute of Techno

²Massachusetts Institute of Technology

April 26, 2024

Abstract

Seismic and geodetic observations show that slow slip events (SSEs) in subduction zones can happen at all temporal and spatial scales and propagate at various velocities. Observation of rapid tremor reversals (RTRs) indicates back-propagating fronts traveling much faster than the main rupture front. Heterogeneity of fault properties, such as fault roughness, is a ubiquitous feature often invoked to explain this complex behavior, but how roughness affects SSEs is poorly understood. Here we use quasi-dynamic seismic cycle simulations to model SSEs on a rough fault, using normal stress perturbations as a proxy for roughness and assuming rate-and-state friction, with strengthening behavior at high slip rate. SSEs exhibit temporal clustering, large variations in rupture length and propagation speed, and back-propagating fronts at different scales. We identify a mechanism for back propagation: as ruptures propagate through low-normal stress regions, a rapid increase in slip velocity combined with rate-strengthening friction induces stress oscillations at the rupture tip, and the subsequent "delayed stress drop" induces secondary back-propagating fronts. Moreover, on rough faults with fractal elevation profiles, the transition from pulse to crack can also lead to the re-rupture of SSEs due to local variations in the level of heterogeneity. Our study provides a possible mechanism for the complex evolution of SSEs inferred from geophysical observations and its link to fault roughness.

Abstract

Seismic and geodetic observations show that slow slip events (SSEs) in subduction zones can happen at all temporal and spatial scales and propagate at various velocities. Observation of rapid tremor reversals (RTRs) indicates back-propagating fronts traveling much faster than the main rupture front. Heterogeneity of fault properties, such as fault roughness, is a ubiquitous feature often invoked to explain this complex behavior, but how roughness affects SSEs is poorly understood. Here we use quasi-dynamic seismic cycle simulations to model SSEs on a rough fault, using normal stress perturbations as a proxy for roughness and assuming rate-and-state friction, with strengthening behavior at high slip rate. SSEs exhibit temporal clustering, large variations in rupture length and propagation speed, and back-propagating fronts at different scales. We identify a mechanism for back propagation: as ruptures propagate through low-normal stress regions, a rapid increase in slip velocity combined with rate-strengthening friction induces stress oscillations at the rupture tip, and the subsequent “delayed stress drop” induces secondary back-propagating fronts. Moreover, on rough faults with fractal elevation profiles, the transition from pulse to crack can also lead to the re-rupture of SSEs due to local variations in the level of heterogeneity. Our study provides a possible mechanism for the complex evolution of SSEs inferred from geophysical observations and its link to fault roughness.

Plain Language Summary

Aseismic slow slip events (SSEs), which like earthquakes can accommodate plate motions, are observed to happen intermittently, propagate backward, and travel at varying speeds. The rough geometry of faults causes heterogeneous stress distribution, which may be responsible for the complex slip behaviors. Here we use computer simulations and analytical tools to study the propagation of SSEs on rough faults. We find more small SSEs, occurring in short bursts, on a rougher fault. We also reproduce faster back-propagating streaks in simulations, analogous to seismological observations. On a fractal fault, ruptures can transition between slip modes (from inchworm-like to zipper-like) which further induces re-rupturing when propagating from high to low roughness areas. Our study helps quantify the effect of fault roughness and further understand underlying mechanics.

1 Introduction

Slow slip events are aseismic fault slip transients with a slip rate of about 1–100 mm/day (Wech & Bartlow, 2014; Hawthorne et al., 2016; Bletery et al., 2017; Frank et al., 2018; Bletery & Nocquet, 2020). Slow slip events (SSEs) and non-volcanic tremors have been observed worldwide in subduction zones, such as Cascadia, Nankai, and Hikurangi (Rogers & Dragert, 2003; Obara et al., 2004; Wallace, 2020). Several candidate mechanisms for slow slip events have been proposed, such as localized regions of lower normal stress (Liu & Rice, 2005, 2007; Rubin, 2008), fault gouge dilatancy (Segall & Rice, 1995; Segall et al., 2010), a transition to velocity-strengthening at a high slip rate (Hawthorne & Rubin, 2013a; Im et al., 2020), and frictional fault embedded within a viscous shear zone (Lavie et al., 2013; Yin et al., 2018; Behr et al., 2021).

Slow slip events exhibit remarkable spatio-temporal complexity. Frank (2016) and Frank et al. (2018) reveal smaller SSEs hidden within the interseismic periods and large events, respectively (also see Rousset et al. (2019)). They also find SSEs are clustered, similar to a cascade of aftershocks following the mainshock (Jolivet & Frank, 2020). Jolivet et al. (2015) and Hawthorne and Bartlow (2018) suggest that the moment of SSEs follows a power law distribution, which resembles Gutenberg-Richter law. The rupture style of SSEs, and the magnitude-duration scaling, are still subjects to debate. SSEs from different regions show a linear moment-duration scaling (Peng & Gomberg, 2010; Gao et

63 al., 2012), associated with pulse-like rupture along an elongated fault (as inferred by Bartlow
 64 et al. (2011) and Radiguet et al. (2011)). On the other hand, events from a single region
 65 follow a duration-cubed scaling like earthquakes (Michel et al., 2019), reminiscent of crack-
 66 like propagation.

67 With advances in seismic and geodetic observations, uncommon slow slip behav-
 68 iors have been identified, and propagation velocities have been better measured. Wech
 69 and Bartlow (2014) use GPS measurement and locations of tremors to find that SSEs
 70 can rupture the same region again with a gap of about 3 weeks by bifurcating into bi-
 71 lateral propagation fronts in Cascadia. Yamashita et al. (2015) observe a re-rupturing
 72 event represented by migrating tremors several days after the first event in the Nankai
 73 subduction zone. Houston et al. (2011) and Obara et al. (2012) observed even faster back-
 74 propagating streaks represented by rapid tremor reversals (RTRs) in the Cascadia, and
 75 Nankai subduction zones, which have also been confirmed with borehole strainmeters (Hawthorne
 76 et al., 2016) and analysis of low-frequency earthquakes (Bletery et al., 2017).

77 These complex slip patterns are likely a manifestation of frictional behavior, fault
 78 heterogeneity, or the interplay between the two. As such, they offer an opportunity to
 79 understand the underlying physical mechanism for slow slip events and constrain fault
 80 properties in the environment of SSEs. Previous models incorporating heterogeneity typ-
 81 ically assume spatial variations in frictional properties: velocity weakening (VW) asper-
 82 ities embedded in a velocity strengthening (VS) fault, producing localized stick-slip be-
 83 havior on a creeping fault (e.g., Luo and Liu (2021)). Other studies employ a velocity-
 84 cutoff model with a transition from velocity weakening to velocity strengthening behav-
 85 ior with increasing slip rate and introduce heterogeneity by varying the cutoff-velocity
 86 (Peng & Rubin, 2018). While the existence of mixed-mode behavior at depths correspond-
 87 ing to SSEs is supported by observations (Behr & Bürgmann, 2021; Kirkpatrick et al.,
 88 2021), their spatial distribution is not well constrained, and modeling studies have ap-
 89 proximated them by placing asperities at random locations, or on a grid (Peng & Ru-
 90 bin, 2018; Luo & Ampuero, 2018). Additionally, several mechanisms have been proposed
 91 to explain back propagation and rapid tremor reversals, such as tidal modulation (Hawthorne
 92 & Rubin, 2013b), fluid pressure wave (Cruz-Atienza et al., 2018; Yin, 2018), fault het-
 93 erogeneity (Luo & Ampuero, 2018; Luo & Liu, 2021), and fault damage zone (Idini &
 94 Ampuero, 2020).

95 Fault roughness represents a ubiquitous and well-characterized source of hetero-
 96 geneity, and like other heterogeneities described above, it can modulate fault stability
 97 (Cattania & Segall, 2021). The migrations of tremors in the Nankai subduction zone ex-
 98 hibit spatial variations of predominant directions (either along strike or dip), as shown
 99 in Sagae et al. (2023). This implies that structural heterogeneities, like fault roughness,
 100 play a significant role due to their known anisotropic properties (Renard & Candela, 2017),
 101 rather than just material differences. Furthermore, it is well established that fault rough-
 102 ness controls the spatial distribution of fault normal stresses (Fang & Dunham, 2013;
 103 Romanet et al., 2020; Cattania & Segall, 2021), and the effect of normal stress pertur-
 104 bations depends on the ratio of normal stress perturbations to background effective nor-
 105 mal stress. Due to the low normal stress conditions associated with SSEs, the change
 106 of normal stress due to fault roughness may play an important role in controlling their
 107 behavior, making them an ideal setting in which to study the effect of heterogeneity on
 108 fault slip patterns. In this study, we seek to determine the effect of fault roughness on
 109 the complex rupture behaviors during SSEs. We use numerical simulations and fracture
 110 mechanics to address the following question: Can fault roughness explain the spatio-temporal
 111 variety of SSE behavior, back propagation, and re-rupture?

112 After introducing the modeling framework (Section 2), we consider the simple case
 113 of sinusoidal perturbations in normal stress (Section 3.1) and show that heterogeneity
 114 with small wavelength and large amplitudes favors complex slip behaviors including a
 115 variety of rupture dimension, clustering, and forward and backward, fast and slow prop-

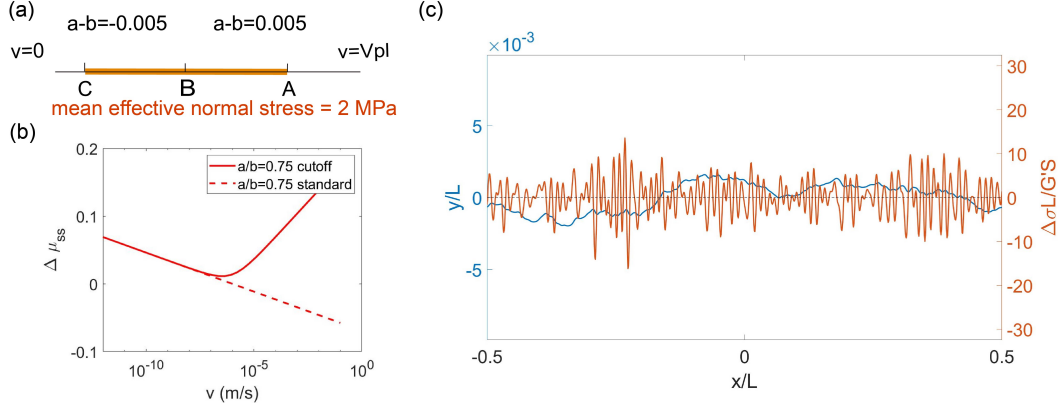


Figure 1. (a) Model geometry. (b) The steady-state friction coefficient of the original rate-and-state friction (dashed line) and velocity cutoff model (solid line, Equation 2). (c) An example of normalized elevation of a rough fault y/L (blue) and perturbation of the normal stress per slip $\Delta \sigma L/G'S$ (red) obtained from Equation 4.

116 agation. Furthermore, we introduce an analytical tool based on fracture mechanics to
 117 explain why SSEs arrest or propagate on a fault with variable normal stress. In Section 3.2,
 118 we discuss a possible mechanism to generate fast-moving back-propagating fronts: a de-
 119 layed stress drop induced by the coupling between normal stress heterogeneity and fric-
 120 tion. Finally, in Section 3.3 we consider a fractal fault, and demonstrate that its irreg-
 121 ular distribution of normal stresses produces dynamics that are not captured by the si-
 122 nusoidal model. In particular, we demonstrate SSE re-rupturing can be induced by a tran-
 123 sition between the pulse to crack-like rupture, as the rupture propagates through regions
 124 of variable local roughness amplitude.

125 2 Models

126 We use the 2D quasi-dynamic boundary element model FDRA (Segall & Bradley,
 127 2012) to simulate SSE cycles on a rough fault. We include normal stress perturbations
 128 as proxies for roughness due to its lower computation cost. The evolution of normal stress
 129 and fault geometry is not considered in this study. Thus, our simulations can be thought
 130 as freeze-frame in the tectonic time scale. This simplification is justified because normal
 131 stress perturbations grow linearly with slip, and a single SSE only increases the total slip
 132 by a small fraction, so that normal stress perturbations do not change significantly dur-
 133 ing several cycles.

134 The model consists of an in-plane fault (mode II) in full space with velocity bound-
 135 ary conditions of tectonic loading rate v_{pl} and 0 at A and C, respectively (Figure 1a; Ta-
 136 ble 1), representing the region between the locked seismogenic zone and steady creep,
 137 where deep SSEs have been observed (Obara et al., 2004; Rogers & Dragert, 2003; Lay
 138 et al., 2012). The fault is composed of a shallow seismogenic (velocity-weakening) region,
 139 BC, and a deep creeping (velocity-strengthening) region, AB. Fault slip is governed by:

$$\tau_{el} = \tau_f + \frac{G}{2c_s}v, \quad (1)$$

140 where τ_{el} is the shear stress due to remote loading and interaction between elements, τ_f
 141 is the frictional resistance, and $\frac{G}{2c_s}v$ is the radiation damping term with shear wave ve-
 142 locity c_s and shear modulus G (Rice, 1993). Slow slip events on a velocity weakening
 143 require a stabilizing mechanism, such a reduction in pore pressure due to slip-induced

Table 1. Model parameters

parameter	value
fault length L	2.5 or 10 km
tectonic loading rate v_{pl}	1×10^{-9} m/s
shear modulus G	3×10^{10} Pa
Poisson's ratio ν	0.25
S wave velocity c_s	3.7×10^3 m/s
friction coefficient μ_0	0.6
reference slip rate v^*	1×10^{-6} m/s
cut-off slip rate v_c	1×10^{-6} m/s
slip rate $v_{\tau-min}$ with minimum steady-state friction	3.33×10^{-7} m/s
friction parameter a for velocity-weakening region	0.015
friction parameter a for velocity-strengthening region	0.025
friction parameter b	0.02
characteristic slip distance D_c	4×10^{-5} m
average normal stress σ_0	2 MPa
amplitude-to-wavelength ratio α_r	0.001
Hurst exponent H	0.7

144 dilatancy (Segall & Rice, 1995) or a transition to velocity strengthening friction with in-
 145 creasing slip velocity, demonstrated in laboratory experiments (Saffer et al., 2001; Ikari
 146 & Saffer, 2011). Here we assume the latter mechanism and employ the velocity-cutoff
 147 model introduced by Hawthorne and Rubin (2013a). Frictional resistance is given by:

$$\tau_f = \left[\mu_1 + a \ln \frac{v}{v^*} + b \ln \left(\frac{\theta v_c}{D_c} + 1 \right) \right] \sigma, \quad (2)$$

148 where $\sigma, \mu_1, v, v^*, \theta, D_c$ and v_c represent normal stress, reference frictional coefficient, slip
 149 rate, reference slip rate, state variable, characteristic slip distance, and cutoff velocity,
 150 respectively. a and b are the coefficients for instant and evolution effects. State evolu-
 151 tion is governed by the aging law (Ruina, 1983) as:

$$\dot{\theta} = 1 - \frac{\theta v}{D_c}. \quad (3)$$

152 In contrast, the original rate-and-state friction is $\mu = \mu_0 + a \ln \frac{v}{v^*} + b \ln \frac{\theta v^*}{D_c}$. To match
 153 two frictional laws at low slip rate, we set μ_1 as $\mu_0 + b \ln \frac{v^*}{v_c}$ (Equation 2). As shown in
 154 Figure 1b, the steady-state friction $\mu_{ss} = \mu_1 + a \ln \frac{v}{v^*} + b \ln \left(\frac{v^*}{v} + 1 \right)$ decreases to a mini-
 155 mum when v reaches $v_{\tau-min} = \frac{b-a}{a} v_c$, and then increases with increasing slip rate, so
 156 that slip instability initiates at $v < v_{\tau-min}$ and does not accelerate into an earthquake
 157 (Figure 1b).

158 The friction parameters a, b, D_c and average normal stress σ_0 we use are shown in
 159 Table 1 and consistent with previous studies (Marone, 1998; Liu & Rice, 2007; Audet
 160 & Kim, 2016). The mean normal stress σ_0 used in the simulations is 2 MPa, which makes
 161 the stress drop $\Delta\tau_{drop}$ about 0.1 MPa, within the range of 0.01 to 1 MPa, consistent with
 162 those inferred by Gao et al. (2012). We impose a perturbation of normal stress, which
 163 mimics the stress heterogeneity on a rough fault with a constant wavelength or a frac-
 164 tal distribution (e.g. Figure 1c). We refer to patches of elevated normal stress as asper-
 165 ities throughout the paper. We set the minimum grid spacing to $\frac{1}{2.5}$ of the smallest co-
 166 hesive zone size L_c to adequately resolve the stress field across the crack tip (Erickson
 167 et al., 2023). The size of cohesive zone L_c is estimated as $1.377 \frac{G' D_c}{b \sigma_{max}^{1-\nu}}$ (Rubin & Ampuero,
 168 2005), where σ_{max} and G' are the maximum normal stress and $\frac{G'}{1-\nu}$, respectively.

169 We use synthetic fractal fault profiles, comparable to natural faults. Faults are cor-
 170 rugated at all scales, and the distribution is self-affine with a Hurst exponent H between
 171 0.4–0.8 (W. Power et al., 1987; Candela et al., 2012; Brodsky et al., 2016; Renard &
 172 Candela, 2017). The fractal fault topography has a power spectrum P^2 proportional to
 173 $(2\pi\lambda)^{-2H-1}$, where λ is the wavelength, and the root-mean-square elevation is given by
 174 $y_{RMS} = \alpha_r \lambda_{max}^H$, where α_r is the amplitude-to-wavelength ratio and λ_{max} is the max-
 175 imum wavelength. For instance, Figure 1c shows a fractal fault with a normalized wave-
 176 length λ/L from 0.01 to 1 and $\alpha_r = 0.001$. We use the following analytical expressions
 177 to relate normal stress perturbations to fault topography (Fang & Dunham, 2013; Cat-
 178 tania & Segall, 2021):

$$\Delta\sigma(x) = \frac{G'S}{2} \mathcal{H}(y'') = \frac{G'S}{2} \int_{-\infty}^{\infty} \frac{y''(\xi)}{x-\xi} d\xi, \quad (4)$$

179 where S is the total slip, and additional shear stress is given by $\Delta\tau(x) = \frac{G'S}{2} y' \mathcal{H}(y'')$,
 180 where $\mathcal{H}(y'')$ is the Hilbert transform of the second derivative of the elevation ampli-
 181 tude y , and S is the accumulated slip. This formula describes $\Delta\sigma$ increases linearly with
 182 S in the elastic regime and does not apply when S is large enough to cause plastic de-
 183 formation or fracturing. The corrugation perturbs the normal stress and shear stress lo-
 184 cally at the scale of the smallest wavelength λ_{min} (Fang & Dunham, 2013; Romanet et
 185 al., 2020; Cattania & Segall, 2021). The root-mean-square (RMS) of normal stress per-
 186 turbation is $\Delta\sigma_{RMS} = (2\pi)^2 \alpha_r \sqrt{\frac{H}{2-H} \frac{G'S}{2} \lambda_{min}^{H-2}}$. While the mean of $\Delta\tau$ is $\Delta\tau_{mean} =$
 187 $(2\pi)^3 \alpha_r^2 \frac{2H}{3-2H} \frac{G'S}{2} \lambda_{min}^{2H-3}$, which is proportional to α_r^2 while $\Delta\sigma_{RMS}$ is proportional to α_r .
 188 The amplitude-to-wavelength ratio α_r of natural faults is about 10^{-3} to 10^{-2} (W. L. Power
 189 & Tullis, 1991). Therefore, we only consider the roughness-induced normal stress per-
 190 turbation $\Delta\sigma$ but not the shear stress $\Delta\tau$ because it is much smaller than $\Delta\sigma$. We use
 191 a slip rate threshold to identify SSEs and to estimate propagation velocities for individ-
 192 ual ruptures and cascading clusters (more detail is provided in section Appendix A).

193 3 Results

194 To obtain insight into how roughness affects slow slip behavior, we first explore the
 195 simple case of sinusoidal perturbations with varying wavelengths and amplitudes; in Sec-
 196 tion 3.3 we consider the more realistic case of normal stresses induced by slip on a frac-
 197 tal fault.

198 3.1 Variety of slip behavior on a sinusoidal rough fault

199 We consider a rough fault with a sinusoidal normal stress distribution with a mag-
 200 nitude given by

$$\sigma(x) = \sigma_0 + \sigma_A \cos \frac{2\pi x}{\lambda}. \quad (5)$$

201 Simulations exhibit a range of SSE behaviors, varying with both wavelength λ and am-
 202 plitude of the normal stress perturbation σ_A . Figure 2 shows a slip behavior as a func-
 203 tion of λ and σ_A/σ_0 . To better highlight differences between simulations, we plot accu-
 204 mulated slip normalized by the theoretical slip profile or a crack driven by end-point dis-
 205 placement (in this case provided by deep creep), given by Rubin (2008):

$$S(x, t) = \frac{S(L, t)}{\pi} \left(\frac{\pi}{2} + \arcsin \frac{x - L/2}{L/2} \right), \quad (6)$$

206 where L , x , and t are the fault length, the location on the fault, and time. We choose
 207 a 2.5 km-long flat fault that is a few times larger than the nucleation length, so that it
 208 only has full ruptures in the homogeneous- σ case (see Cattania (2019)), as shown in Fig-
 209 ure 2a and 2b. In this case, full ruptures are well approximated as a constant stress drop
 210 crack (Figure 2a), with an elliptical slip profile (Eshelby, 1957). Cases with low σ_A/σ_0

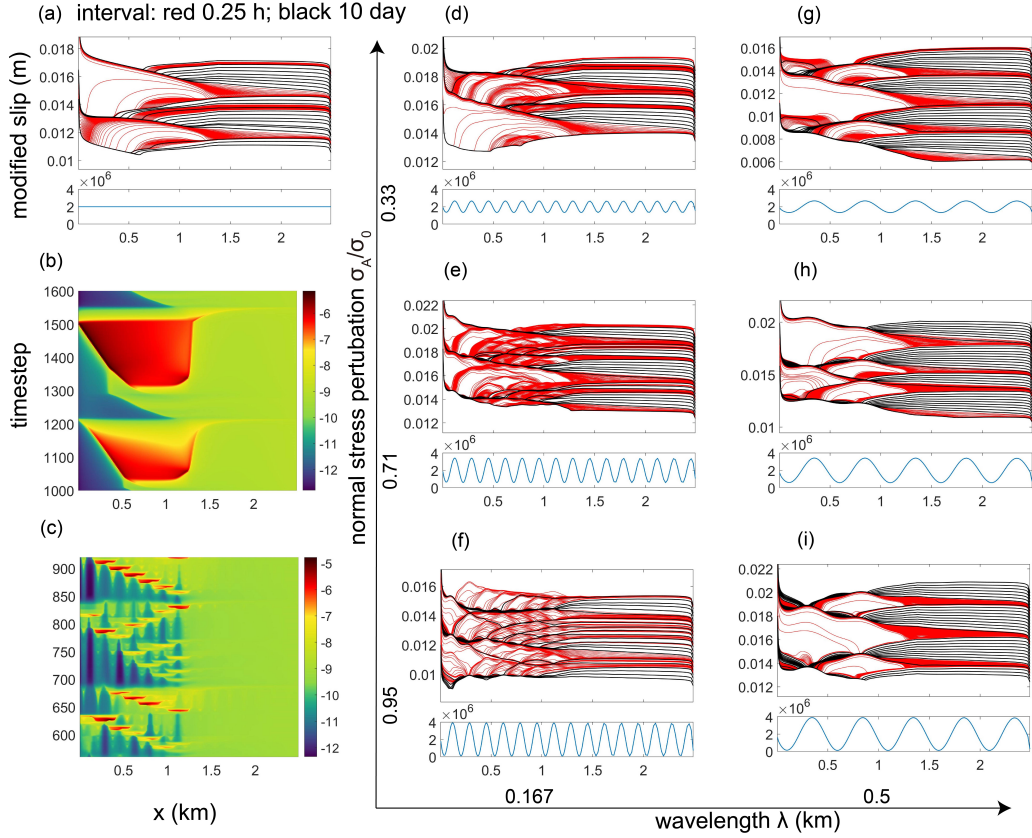


Figure 2. Effect of sinusoidal normal stress perturbations on rupture style. (a) normalized slips with uniform σ . Normalized slip equals slip s divided by $\frac{\pi}{2} + \arcsin \frac{x-W/2}{W/2}$. (d-i) Normalized slip profiles as a function of wavelength (λ) and perturbation amplitude (σ_A/σ_0). (b) and (c) show the slip rate for each time step for cases (a) and (f), respectively.

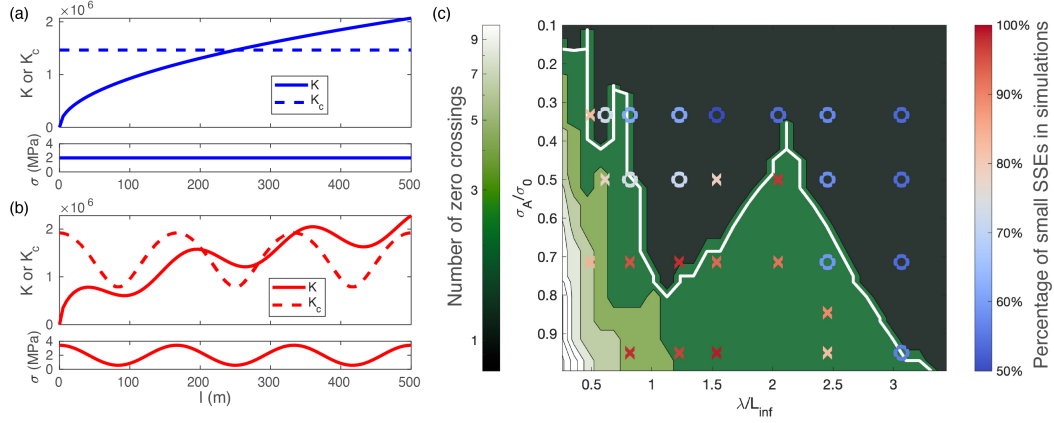


Figure 3. Stress intensity factor K (solid line) and local toughness K_c (dashed line) for the constant (a) and perturbed (b) normal stress. The slip will arrest at $l = 280$ m. (c) Number of zero crossings of $K - K_c$ and percentage of small SSEs in simulations with varying normalized wavelength λ/L_∞ and amplitude-to-constant ratio σ_A/σ_0 . The red contouring line represents the threshold for arresting (3 zero crossings). Colors of circles and crosses represent the percentage of events smaller than 2λ in the simulations with a 2.5 km-long fault (circle: > 0.75 ; cross: < 0.75).

211 and long wavelength exhibit crack-like ruptures and partial ruptures (Figure 2d, 2g and
 212 2h), whereas with the increase of wavenumber and perturbation amplitude σ_A , there are
 213 more pulse-like ruptures composed of localized slip pockets and an overall flat slip pro-
 214 file (Figure 2f). A similar transition from crack to pulse-like rupture due to fault rough-
 215 ness was observed by Heimisson (2020), and interpreted as a consequence of additional
 216 shear resistance from fault roughness (roughness drag; Fang and Dunham (2013)). Our
 217 results indicate that pulse-like rupture can still occur exclusively as a result of a pertur-
 218 bation in normal stress. Each cluster ruptures the whole velocity-weakening region inter-
 219 mittently, and it ruptures more than once in some regions (Figure 2c and 2f). Note
 220 that these partial ruptures are often nucleated at a high- σ region and arrested by the
 221 high- σ regions nearby (Figure 2f and 2i), which have a higher local fracture energy, as
 222 discussed below.

223 3.1.1 Rupture arrest with variable normal stress

224 To get more insight into rupture arrest, we use a fracture mechanics criterion ac-
 225 counting for heterogeneity. Rupture propagation is controlled by the criterion: $K = K_c$,
 226 where K and K_c are stress intensity factor and local toughness, respectively (Griffith,
 227 1921; Irwin, 1957). Normal stress heterogeneity affects both these terms: enhanced com-
 228 pression at the crack tip increases the local toughness K_c , thus favoring rupture arrest;
 229 however, it also increases the stress drop and hence K , which promotes rupture prop-
 230 agation. Analytical calculations are described in Appendix B.

231 Figure 3a and b illustrate examples of K and K_c distributions for constant and per-
 232 turbed normal stress. The zero crossing of $K - K_c$ of a smooth fault (red) is located
 233 at about $l \approx 250$ m, which is similar to the nucleation half length $L_\infty = \frac{G' b D_c}{\pi (b-a)^2 \sigma}$. As
 234 the crack reaches the nucleation dimension, it will grow unstable and propagate indef-
 235 initely as long as the stress drop remains uniform. However, $K - K_c$ has 3 zero cross-
 236 ings for the case with perturbed normal stress (blue). The SSE is likely to nucleate at
 237 the first zero crossing ($l \approx 200$ m) and arrest at the second zero crossing ($l \approx 280$ m)
 238 because it cannot penetrate the high- σ region ($l \approx 280 - 330$ m) where $K < K_c$.

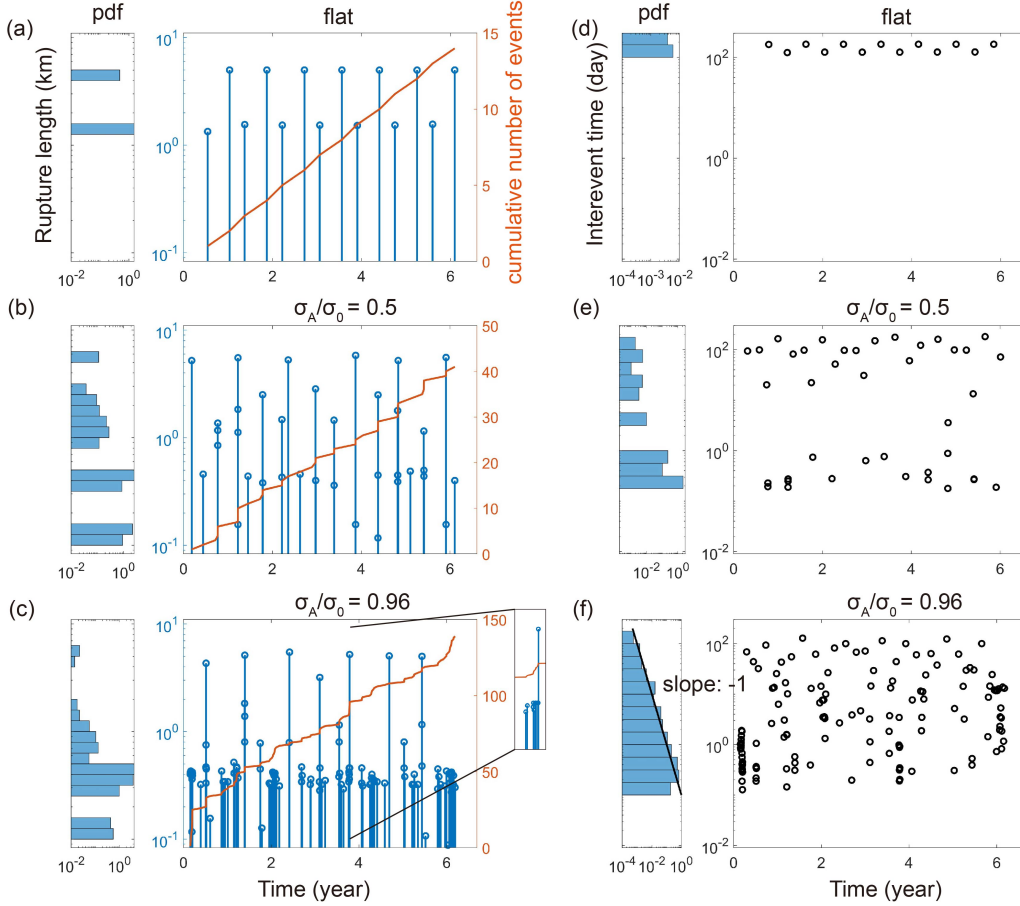


Figure 4. Effect of perturbation amplitude on SSE catalogs. Rupture lengths (a, b, c) and interevent times (d, e, f) with increasing sinusoidal σ perturbation on a 10 km-long fault ($\lambda = 0.33$ km). SSEs are outlined by a threshold of 1×10^{-6} m/s. Events that are closer than the duration of full ruptures are merged as one.

239 Figure 3c shows the conditions under which SSEs might arrest according to this
 240 analysis. Figure 3c excludes the perturbed wavelength shorter than the cohesive zone
 241 ($1.377L_b \approx 55$ m), with $L_b = \frac{G'D_c}{b\sigma}$ (Rubin & Ampuero, 2005; Ampuero & Rubin, 2008),
 242 because local toughness K_c cannot be calculated as Equation B4 due to the varying normal
 243 stress in the cohesive zone. If $K - K_c$ has more than three zero crossings in Figure 3b,
 244 the SSEs tend to stop at the high-normal-stress region and propagate like a pulse
 245 discontinuously. Therefore, the parameter space for arresting is below the white curve,
 246 while the black area indicates that ruptures will not arrest. For the same wavelength λ ,
 247 SSEs are more likely to arrest if the normal stress perturbation is larger. The range of
 248 wavelength promoting rupture arrest is narrow for smaller normal stress perturbations.
 249 We also compare our analytical model with the percentage of SSEs smaller than 2λ
 250 in the simulations (several cases are shown in Figure 2) since there are more small SSEs
 251 if arresting happens more frequently. The cross indicates that most SSEs ($> 75\%$) are
 252 small, while the circle indicates fewer small ruptures ($< 75\%$). To first order, the dis-
 253 tribution of crosses and circles shows a Z-shaped boundary and our model aligns with
 254 simulations. This analysis demonstrates that the strong spatial variations of both local
 255 toughness K_c and stress intensity factor K of potential ruptures along the rough fault
 256 can account for the breakdown of a single large SSE into multiple smaller SSEs.

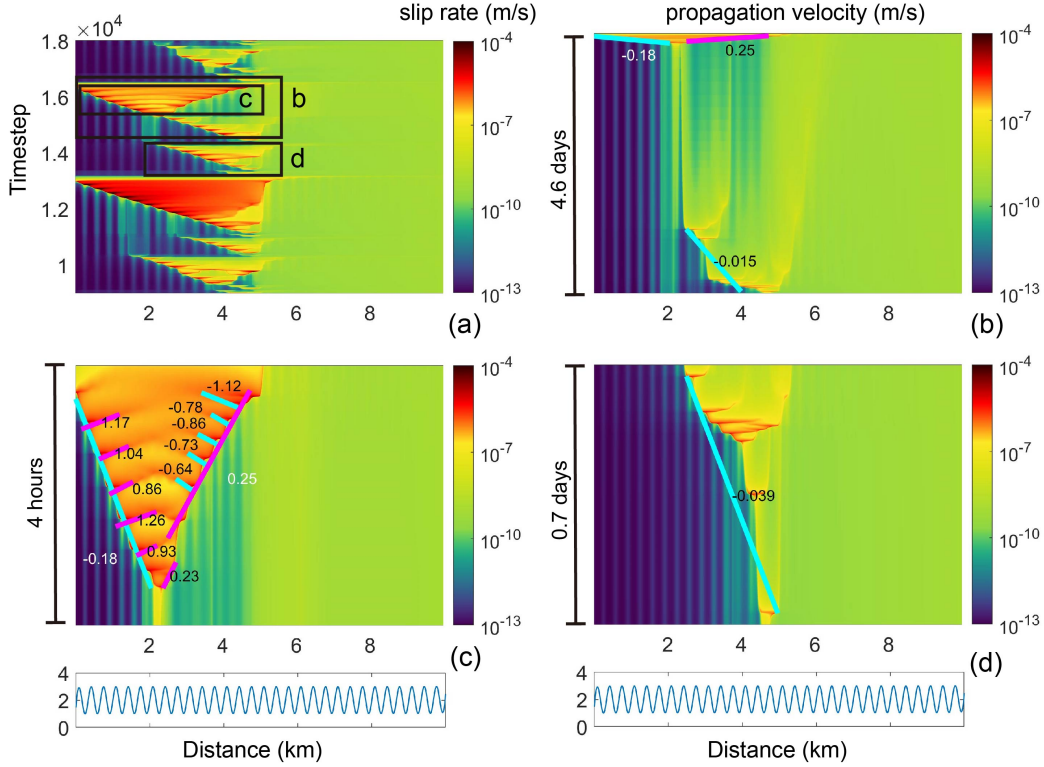


Figure 5. Evolution of SSE cycles (a), consisting of pre-slips plus full rupture (b), full rupture with back-propagating fronts (c) and clustered subevents (d) and normal stress distribution with $\lambda = 0.33$ km and $\sigma_A/\sigma_0 = 0.5$. The fitting lines for updip and downdip propagation are in light blue and pink respectively and the corresponding velocity is noted beside (unit: m/s). The threshold slip rate for outlining events is 1×10^{-6} m/s.

257

3.1.2 Temporal statistics and size distribution

258

259

260

261

262

263

264

265

266

267

268

269

270

271

272

273

The SSE catalogs simulated on a fault with higher roughness show more randomness and clustering (Figure 4). Figure 4a and d exhibit stable SSE cycles consisting of a full rupture and a partial rupture on a 10 km-long flat fault. However, for the rough fault, Figure 4b and c shows a larger number of SSEs with increasing amplitude of σ perturbations, consistent with the analysis in the previous section. The SSE interevent time catalog for the case with $\sigma_A/\sigma_0 = 0.5$ shows two groups of intervals of about 100 days and 1 hour (Figure 4b), corresponding to the time between full rupture and subsequent cluster, and the time between subevents within pre-slip and subsequent clusters, respectively. However, the case with a higher $\sigma_A/\sigma_0 = 0.96$ exhibits more continuously distributed intervals spanning four orders of magnitude, from 10 minutes to 100 days (Figure 4c), with temporal clustering around the largest events. More small SSEs also appear on faults with higher roughness (Figure 4e and 4f). A cluster of small events can cause less uniform background stress, so the rupture length and time for the next event are less predictable. This result is similar to the observations showing that a large SSE can be decomposed into a cluster of smaller events (Jolivet et al., 2015; Frank, 2016; Frank et al., 2018; Rousset et al., 2019; Jolivet & Frank, 2020).

274

3.1.3 Rupture velocities

275

276

277

278

279

280

281

282

283

284

285

286

287

Fault roughness also promotes a range of propagation directions and velocities. Figure 5a shows that one SSE cycle on a rough fault is composed of a cluster of pre-slips (Figure 5b), full rupture (Figure 5c) and clustered subevents (Figure 5d). The dimension of subevents is one to several wavelengths, and they are confined by asperities. The clusters usually start from the boundary of the seismogenic and creeping regions and generally propagate updip intermittently, but sometimes propagate downdip (Figure 5b and 5d). Full ruptures usually nucleate at the end of the cluster of pre-slips (Figure 5b). The updip and downdip propagations of full ruptures exhibit similar velocities: 0.18 and 0.25 m/s (15.5 and 21.6 km/day). However, the propagation velocities of the pre-slip cluster and the subsequent events are smaller than that of the full rupture by a factor of 5–10. This smaller velocity can be explained by the lower state variable θ : in the cluster of pre-slips and subsequent events, the event in the front is not triggered immediately because it is still below steady-state after the stress change.

288

3.2 Back propagating fronts

289

290

291

292

293

A common feature in rough fault simulations is the occurrence of fast back-propagating fronts within a full rupture (Figure 5c). Their propagation velocity is 3–7 times higher than the forward propagation. These secondary ruptures may be analogous to rapid tremor reversals (Houston et al., 2011) or fast streaks observed along dip (Shelly et al., 2007; Ghosh et al., 2010).

294

295

296

297

298

299

300

301

302

303

304

305

306

307

308

309

310

311

312

To understand the origin of back-propagating fronts, in Fig. 6 we compare the evolution of stress and slip velocities on flat and rough faults. On a smooth fault, the crack tip stress and velocity profiles are simply translated as the rupture propagates, and a constant stress drop within the rupture drives the crack at constant velocity (Figure 6a). On the other hand, propagation along rough faults induces large fluctuations in slip velocity and stress drop: the missing piece of the puzzle is a temporary positive stress change $\Delta\tau$ behind the crack tip, that enables ruptured asperities to break again and trigger a secondary slip front. We use the term “delayed stress drop” to describe this mechanism for back-propagating fronts on rough faults, which can be understood in the framework of rate-and-state friction law and velocity-cutoff model. In the case of forward propagation at the crack-tip, the slip rate in the low- σ region is significantly higher than that in the high- σ region (Figure 6d). When the rupture front passes the low- σ region, the slip rate on the asperity behind is also elevated to a similar level as the low- σ region (profile 3 in Figure 6d), which causes the shear stress to increase due to velocity-strengthening behavior at higher slip rate (Figure 1b, profile 3 in Figure 6c). As the rupture propagates into high σ regions, the slip velocity and stress decrease, as shown by the difference between stress profiles 4 and 3 (solid black line in Figure 6c). This delayed stress drop causes a stress increase on the asperities behind ($x \approx 800$ m and $x \approx 1300$ m), and hence induce secondary back propagation in its wave.

313

3.3 Pulse-to-crack transition and re-rupture on fractal faults

314

315

316

317

318

319

320

321

322

On a fractal fault, heterogeneity varies more randomly than in the sinusoidal cases presented above: since the local amplitude and (to a lesser extent) frequency content varies spatially, the slip regimes displayed in Figure 2 can all coexist on a single fault surface, and slip front propagation across these different regimes generates additional complexity. Figure 7 shows a case with a fractal rough fault with wavelength λ between 0.125 and 10 km and Hurst exponent $H = 0.7$. Within a single full rupture (about one day long), there are two kinds of rupture behaviors, first pulse-like and then crack-like. Additionally, some even faster “streaks” propagate backward in the simulations, analogous to be behavior discussed in section 3.2.

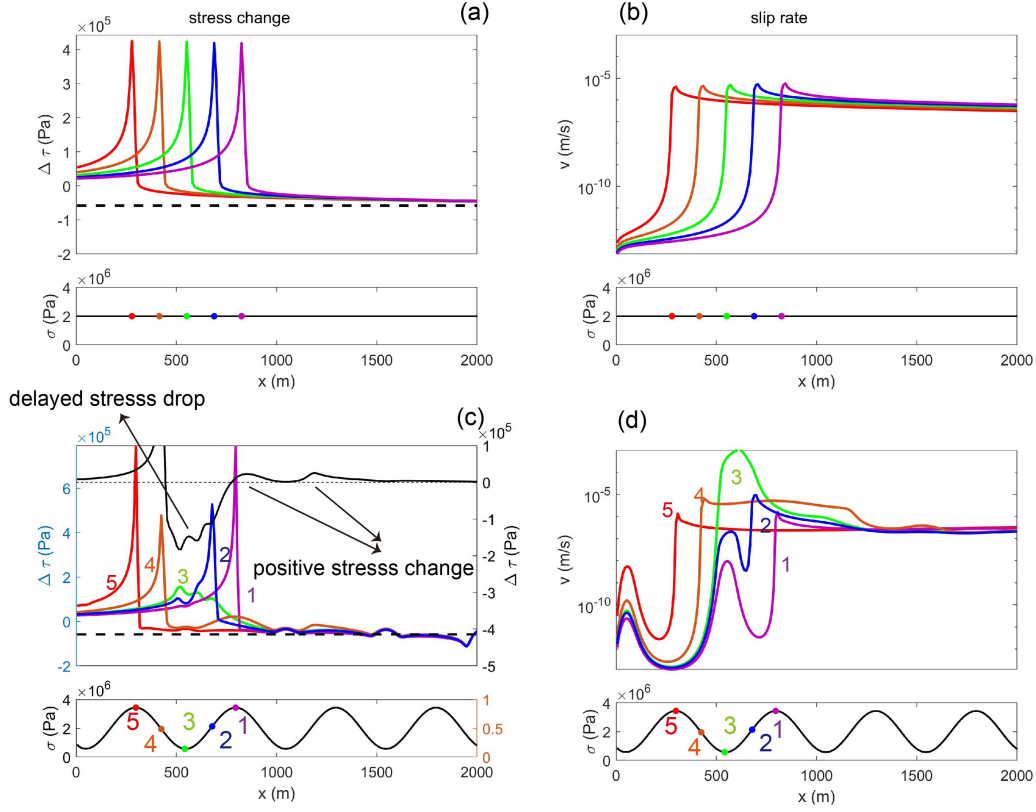


Figure 6. Stress change and slip rate profile along a flat fault (a and b) or fault with sinusoidal normal stress (c and d; $\lambda = 0.5$ km and $\sigma_A/\sigma_0 = 0.71$) when the rupture propagates from right to left. Colored lines represent profiles when the crack tips are at the extrema and mean of σ (c and d; coded by 1 to 5). The black line in (c) represents the difference between stress profiles 4 and 3. The dashed line represents the stress change after an event.

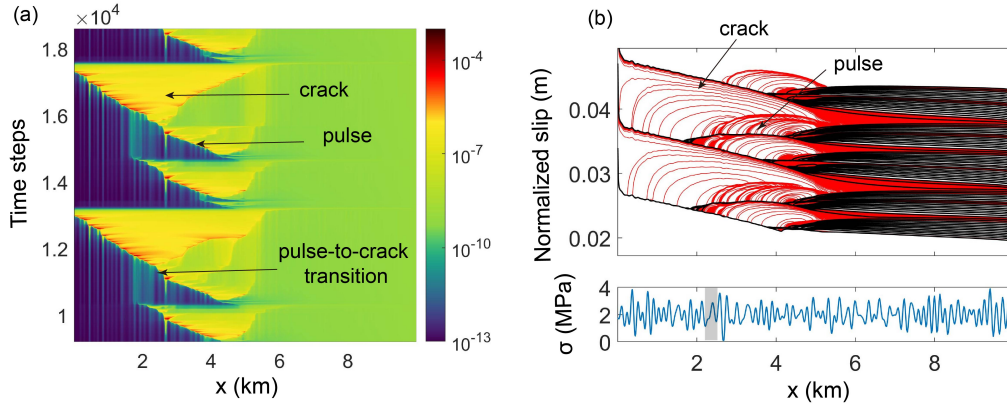


Figure 7. Slip behaviors on a fractal fault. (a) Slip rate across two SSE cycles. (b) Top: normalized slip along the fault during several SSE cycles, (cumulative slip divided by $\frac{\pi}{2} + \arcsin \frac{x-W/2}{W/2}$). The black lines represent interseismic slip with an interval of around 10 days. Red lines are plotted with an interval of 0.25 hour when the maximum slip rate is larger than v_{pl} . Bottom: distribution of the normal stress obtained from Equation 4 with $S = 55$ mm. The grey box denotes where the pulse-to-crack transition happens.

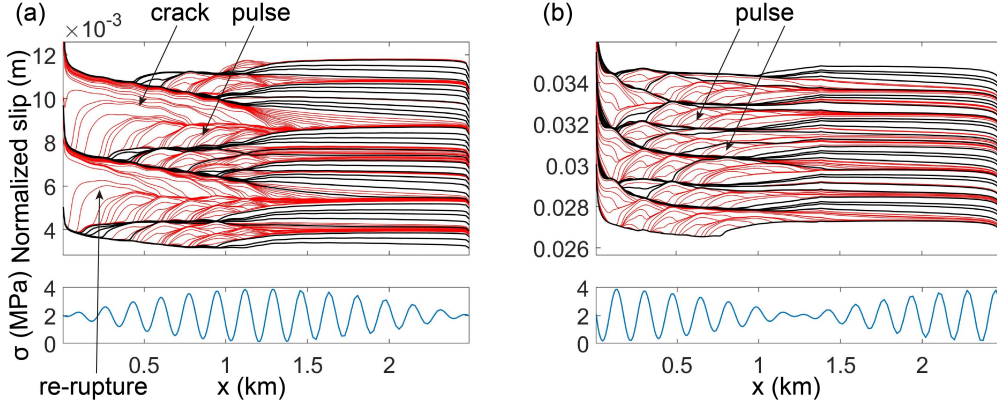


Figure 8. Normalized slip and normal stress for “walnut” case (a) and “hourglass” (b). (a) Re-rupture within a full-rupture event which propagates from high to low roughness regions. (b) SSEs propagating as a pulse from low to high roughness regions without re-rupture.

323 In Figure 7, pulse-like ruptures are usually clusters of small sub-events and propa-
 324 gate slowly, while crack-like ones are single extensive events and propagate much faster.
 325 As shown in section 3.1 and Figure 2, the amplitude of normal stress perturbations deter-
 326 mines whether a rupture propagates as a crack or a pulse. Therefore, we proposed that
 327 the transition from pulse to crack is caused by spatial variations of normal stress: higher
 328 amplitudes of normal stress perturbations favor pulse-like ruptures, so pulse-to-crack tran-
 329 sitions can take place as rupture propagates into regions with lower local roughness.

330 To test this, we compare two end-member cases of a “walnut” and an “hourglass”
 331 normal stress perturbation (Figure 8) to study how the local amplitude of the pertur-
 332 bation affects rupture propagation. We construct the normal stress perturbation with
 333 two sinusoidal functions of similar wavelengths, $0.179 \left(\frac{2.5}{14}\right)$ and $0.167 \left(\frac{2.5}{15}\right)$ km, with a
 334 group wavelength of 2.5 km. We find that day-long single events exhibit the pulse-to-
 335 crack transition and re-rupture in the “walnut” case (Figure 8a), in which the SSE propa-
 336 gates from high roughness to low roughness areas. Ruptures initiate as pulses in the
 337 region with a larger perturbation amplitude ($x \approx 1.25$ km) and evolve into cracks in
 338 the region with nearly constant normal stress ($x \approx 0$ km). We interpret this as caused
 339 by the deficit between crack and pulse-like slip profiles, a mechanism that was previously
 340 identified by Idini and Ampuero (2020) for faults surrounded by a damage zone. In prin-
 341 ciple, the slip deficit could also be filled with subsequent small SSEs as shown in Fig-
 342 ure 8b. We suggest that it is also easier for the re-rupture to penetrate the lower-roughness
 343 region ($x \approx 0$ km) due to absence of strong asperities, so that a single full rupture is
 344 favored. In contrast, ruptures remain pulse-like when propagating from the low into the
 345 high roughness region in the “hourglass” case (Figure 8b), which usually last on the or-
 346 der of 10 days. The presence of high normal stress (asperities) in the high roughness re-
 347 gion ($x \approx 0$ km) also prevents this area from re-rupturing in a single events, as Figure
 348 8a.

349 4 Discussion

350 In this study, we analyze how heterogeneous normal stress induced by fault rough-
 351 ness produces rich slip behavior during slow slip events. We reproduce SSEs with a range
 352 of rupture lengths on rough faults in the simulations, which is consistent with geodetic
 353 observations that show a power-law distribution of the sizes of slip bursts on a rough fault
 354 (Jolivet et al., 2015; Hawthorne & Bartlow, 2018), and is similar to an emerging cascade

355 of slow slips and foreshocks on rough faults from numerical simulations (Cattania & Segall,
 356 2021). Our simulations also exhibit clustering behaviors that a long-period SSE can be
 357 decomposed into several short subevents, which is analogous to the observations such
 358 as Frank et al. (2018) and Rousset et al. (2019). We suggest that fault roughness, a uni-
 359 versal characteristic in nature, can explain many complex dynamics of SSEs. This com-
 360 plexity can be simply understood within the context of linear elastic fracture mechan-
 361 ics.

362 Simulations show complex rupture behaviors on rough faults, including forward and
 363 back propagation at varying speeds, which differ from that on flat and frictionally uni-
 364 form faults. We observe strongly-varying slip rates when the rupture front first passes
 365 low and high normal stress regions, in contrast to roughly constant slip rate behind back-
 366 propagating fronts. The difference can be explained by initial conditions (state variable
 367 and slip rate), which are strongly heterogeneous ahead of the rupture front, and more
 368 uniform within the rupture itself. Together with a velocity-cutoff model, this varying crack-
 369 tip slip rate can also induce a delayed stress drop on the asperity behind, which causes
 370 back propagation.

371 Observations indicate that only certain areas experience repeated RTRs with simi-
 372 lar directions, and the propagation velocity differs across locations (Sagae et al., 2023).
 373 This points to spatial variations in roughness as a potential reason. Future studies can
 374 use the distributions of RTRs, propagation velocity, and high-energy radiators (asper-
 375 ities) to test this hypothesis. Simulations that include a heterogeneous asperities-in-matrix
 376 fault also produce back propagation (Luo & Liu, 2021; Peng & Rubin, 2018; Nie & Bar-
 377 bot, 2021). The presence of unstable patches embedded in a stable matrix will produce
 378 variations in stress drops when ruptures cross patches with different frictional proper-
 379 ties, perhaps analogous to the “delayed stress drop” we observed here. Although our sim-
 380 ulations are limited to rate-state friction, the mechanism we identified may also apply
 381 to other cases, as long as two conditions are met. The first is the presence of heteroge-
 382 neous fault properties (such as geometry or friction), capable of efficiently modulating
 383 slip rate along the rupture front. The second is a rate-strengthening mechanism, oper-
 384 ating on a sufficiently short time scale to allow for fast restrengthening and subsequent
 385 stress release upon deceleration, so that a back-propagating front can be triggered. Fur-
 386 ther studies are need to verify whether other stabilizing mechanisms, such as fault dil-
 387 atancy (Segall & Rice, 1995), indeed produce similar behavior.

388 Our simulations show a wide range of propagation velocities. Specifically, the prop-
 389 agation velocity of clustering subevents, forward and back-propagating fronts are on the
 390 order of 0.01, 0.1 and 1 m/s, respectively. SSEs generally travel at about 0.1 m/s; how-
 391 ever, certain SSEs in Japan and Mexico demonstrate a slower pace of about 0.01 m/s
 392 (Gao et al., 2012). Back propagation velocities observed in nature are about 1–5 and
 393 7 – 40 m/s for rapid tremor reversals and along-dip streaks, respectively (Houston et
 394 al., 2011; Shelly et al., 2007; Ghosh et al., 2010). While our simulations accurately cap-
 395 ture the speeds of forward propagation, they seem to underestimate the back-propagating
 396 ones. This implies that the friction parameters in nature are different from those used
 397 in our model or that another unknown mechanism controls this process. We will address
 398 this problem by exploring a broader region of parameter space and developing theoret-
 399 ical formulas in future studies.

400 In addition to back-propagating fronts, fractal faults exhibit sustained, large-scale
 401 re-ruptures. We have identified a mechanism for this behavior, caused by the more ir-
 402 regular roughness distribution on a fractal fault compared to the sinusoidal case, which
 403 can induce pulse-to-crack transitions. Furthermore, natural faults are more complex as
 404 the roughness varies spatially on the same surface indicated by the 3D seismic reflection
 405 (Kirkpatrick et al., 2020) and Lidar observation (Candela et al., 2009). It is easier to in-
 406 duce re-rupture due to the transition from pulse to crack when SSEs propagate from high
 407 roughness to low roughness region. Sagae et al. (2023) shows that the occurrence of sec-

408 ondry tremor migrations depends on the directions of the primary rupture front. Our
 409 mechanism is among the few that offer an explanation for this observation. The pulse-
 410 to-crack transition mediated by roughness is not specific to slow slip, and it may be ap-
 411 plied to a recently observed “boomerang earthquake”, which propagates back through
 412 the initial rupture area (Hicks et al., 2020; S. Yamashita et al., 2022).

413 5 Conclusion

414 We find clustering of slow slip events, different rupture lengths, and varying prop-
 415 agation velocities on a rough fault in the simulations. SSEs tend to arrest and propa-
 416 gate intermittently, which generates a pulse-like slip profile when roughness is high, and
 417 the amplitude of the normal stress perturbation is large. The secondary back propaga-
 418 tion can be induced by fault restrengthening followed by a delayed stress drop when the
 419 rupture passes a low normal stress region. Finally, we find that the transition from pulse
 420 to crack can lead to a large scale re-rupture and back propagation when SSEs propagate
 421 from high to low roughness regions on a fractal fault.

422 Acknowledgments

423 The authors thank Jared Bryan, Xin Cui, William Frank, Zhi Li, Enrico Milanese, and
 424 Qing-Yu Wang for helpful discussions. Y.S. received fundings from MIT EAPS Robert
 425 R Shrock Fellowship, Sven Treitel (1953) Fellowship, and MIT Mathworks Fellowship.

426 Appendix A Estimating propagation velocities

427 To calculate propagation velocity, we used two methods: one for a single event, and
 428 one for clusters of several events. The first method is to use a slip rate threshold to out-
 429 line events and fit the rupture fronts linearly to calculate updip and downdip propaga-
 430 tion velocity (e.g. full rupture in Figure 5b). We can also increase the threshold to de-
 431 lineate the back-propagating fronts and calculate their velocities. We may not capture
 432 all the back-propagating fronts using one threshold, so we use several thresholds and choose
 433 the most representative velocity by visual inspection.

434 Figure 2f also shows clusters of intermittent events that produce a “fish-scale” pat-
 435 tern with each event arresting on a high normal-stress patch. To estimate the propaga-
 436 tion velocity of these clusters, we first outline the subevents by a threshold near the cut-
 437 off velocity (1×10^{-6} m/s). Then we identify clusters as groups of subevents with the
 438 interevent time less than 3 days, which separates the two peaks of the bimodal inter-event
 439 time distribution in Figure 4b. Finally, we use the uppermost/lowermost end of every
 440 event to calculate the updip/downdip propagation velocity of the cluster (e.g. pre-slips
 441 in Figure 5b and subsequent events in Figure 5d).

442 Appendix B Criterion for rupture propagation and arrest

443 In Figure 2, ruptures show pulse-like behavior and stop in high- σ region because
 444 the local toughness there is higher. Here we present a fracture mechanics analysis to ex-
 445 plain rupture propagation and arrest under heterogeneous normal stress. For simplic-
 446 ity, we neglect rupture arrest caused by gradients in the background stress field due to
 447 loading from deep creep (Cattania, 2019). SSEs are mostly nucleated at peaks of nor-
 448 mal stress, so we consider a crack extending from the normal stress maximum at $x =$
 449 0 (eq. 5) to the crack tip at $x = l$ to obtain stress intensity factor K (Tada et al., 1973)
 450 as a function of the stress drop $\Delta\tau$:

$$K = \int_0^l \frac{\sqrt{2}}{\sqrt{\pi(l-x)}} \Delta\tau(x) dx = 2\sqrt{\frac{2l}{\pi}} \Delta\tau_0 + \sqrt{\frac{2\lambda}{\pi}} \Delta\tau_A \left[C(2\sqrt{\frac{l}{\lambda}}) \cos \frac{2\pi l}{\lambda} + S(2\sqrt{\frac{l}{\lambda}}) \sin \frac{2\pi l}{\lambda} \right],$$

$$S(x) = \int_0^x \sin \frac{\pi t^2}{2} dt,$$

$$C(x) = \int_0^x \cos \frac{\pi t^2}{2} dt, \quad (\text{B1})$$

451 where $S(x)$ and $C(x)$ are Fresnel integrals. In Equation B1, $\Delta\tau$ is assumed proportional
 452 to normal stress (Equation 5), with $\Delta\tau_0$ and $\Delta\tau_A$ due to the constant and sinusoidal terms
 453 respectively. The stress drop equals the difference between the initial and minimum fric-
 454 tional stress as:

$$\Delta\tau_{0,A} = \sigma_{0,A} \left(-a \ln \frac{v_{\tau-min}}{v_i} + b \ln \frac{v_c \theta_i / D_c + 1}{v_c / v_{\tau-min} + 1} \right), \quad (\text{B2})$$

455 where v_i and θ_i are the initial slip rate and initial state variable, respectively. In sim-
 456 ulations, the slip rate is $v_i \approx v_{pl}$ in the nucleation zone and it is near steady state as
 457 $v_i \theta_i / D_c = 1$.

458 The local toughness K_c is calculated from the fracture energy G_c as $G_c = \frac{K_c^2}{2G'} =$
 459 $\frac{D_c}{2b\sigma} (\Delta\tau_{p-r})^2$, where $\Delta\tau_{p-r}$ is the peak to residual stress drop. Hawthorne and Rubin (2013a)
 460 derived the stress drop for the velocity-cutoff model as

$$\Delta\tau_{p-r} = b\sigma \left[\ln \left(\frac{v_c \theta_i / 2}{D_c} + 1 \right) - \ln \left(\frac{v_c}{v_{max}/2} + 1 \right) \right]. \quad (\text{B3})$$

461 Thus, K_c is given by

$$K_c = \sqrt{G' b \sigma D_c} \left[\ln \left(\frac{v_c \theta_i / 2}{D_c} + 1 \right) - \ln \left(\frac{v_c}{v_{max}/2} + 1 \right) \right]. \quad (\text{B4})$$

462 To simplify, we use $\theta_i = D_c / v_{pl}$, which represents the creeping region, for K_c all along
 463 the fault. This choice is made because K and K_c have a phase difference of about $\pi/2$,
 464 with the second zero crossing frequently occurring within the creeping region (Figure 3).
 465 Additionally, both the high and low- σ regions undergo creeping following the first rup-
 466 ture.

467 Open Research Section

468 We use MATLAB to plot figures. The results of our simulations (Figure 2, 5 and
 469 7) and simulated SSE catalogs (Figure 4) are archived in Zenodo (Sun & Cattania, 2024).

References

470

- 471 Ampuero, J.-P., & Rubin, A. M. (2008). Earthquake nucleation on rate and state
472 faults—aging and slip laws. *Journal of Geophysical Research: Solid Earth*,
473 *113*(B1).
- 474 Audet, P., & Kim, Y. (2016). Teleseismic constraints on the geological environ-
475 ment of deep episodic slow earthquakes in subduction zone forearcs: A review.
476 *Tectonophysics*, *670*, 1–15.
- 477 Bartlow, N. M., Miyazaki, S., Bradley, A. M., & Segall, P. (2011). Space-time corre-
478 lation of slip and tremor during the 2009 cascadia slow slip event. *Geophysical*
479 *Research Letters*, *38*(18).
- 480 Behr, W. M., & Bürgmann, R. (2021). What’s down there? the structures, materi-
481 als and environment of deep-seated slow slip and tremor. *Philosophical Trans-*
482 *actions of the Royal Society A*, *379*(2193), 20200218.
- 483 Behr, W. M., Gerya, T. V., Cannizzaro, C., & Blass, R. (2021). Transient slow slip
484 characteristics of frictional-viscous subduction megathrust shear zones. *AGU*
485 *Advances*, *2*(3), e2021AV000416.
- 486 Bletery, Q., & Nocquet, J.-M. (2020). Slip bursts during coalescence of slow slip
487 events in cascadia. *Nature communications*, *11*(1), 1–6.
- 488 Bletery, Q., Thomas, A. M., Hawthorne, J. C., Skarbek, R. M., Rempel, A. W., &
489 Krogstad, R. D. (2017). Characteristics of secondary slip fronts associated
490 with slow earthquakes in cascadia. *Earth and Planetary Science Letters*, *463*,
491 212–220.
- 492 Brodsky, E. E., Kirkpatrick, J. D., & Candela, T. (2016). Constraints from fault
493 roughness on the scale-dependent strength of rocks. *Geology*, *44*(1), 19–22.
- 494 Candela, T., Renard, F., Bouchon, M., Brouste, A., Marsan, D., Schmittbuhl, J.,
495 & Voisin, C. (2009). Characterization of fault roughness at various scales:
496 Implications of three-dimensional high resolution topography measurements. In
497 *Mechanics, structure and evolution of fault zones* (pp. 1817–1851). Springer.
- 498 Candela, T., Renard, F., Klinger, Y., Mair, K., Schmittbuhl, J., & Brodsky, E. E.
499 (2012). Roughness of fault surfaces over nine decades of length scales. *Journal*
500 *of Geophysical Research: Solid Earth*, *117*(B8).
- 501 Cattania, C. (2019). Complex earthquake sequences on simple faults. *Geophysical*
502 *Research Letters*, *46*(17-18), 10384–10393.
- 503 Cattania, C., & Segall, P. (2021). Precursory slow slip and foreshocks on rough
504 faults. *Journal of Geophysical Research: Solid Earth*, *126*(4), e2020JB020430.
- 505 Cruz-Atienza, V. M., Villafuerte, C., & Bhat, H. S. (2018). Rapid tremor migration
506 and pore-pressure waves in subduction zones. *Nature communications*, *9*(1), 1–
507 13.
- 508 Erickson, B. A., Jiang, J., Lambert, V., Barbot, S. D., Abdelmeguid, M., Almquist,
509 M., ... others (2023). Incorporating full elastodynamic effects and dipping
510 fault geometries in community code verification exercises for simulations of
511 earthquake sequences and aseismic slip (seas). *Bulletin of the Seismological*
512 *Society of America*, *113*(2), 499–523.
- 513 Eshelby, J. D. (1957). The determination of the elastic field of an ellipsoidal inclu-
514 sion, and related problems. *Proceedings of the royal society of London. Series*
515 *A. Mathematical and physical sciences*, *241*(1226), 376–396.
- 516 Fang, Z., & Dunham, E. M. (2013). Additional shear resistance from fault rough-
517 ness and stress levels on geometrically complex faults. *Journal of Geophysical*
518 *Research: Solid Earth*, *118*(7), 3642–3654.
- 519 Frank, W. B. (2016). Slow slip hidden in the noise: The intermittence of tectonic re-
520 lease. *Geophysical Research Letters*, *43*(19), 10–125.
- 521 Frank, W. B., Rousset, B., Lasserre, C., & Campillo, M. (2018). Revealing the clus-
522 ter of slow transients behind a large slow slip event. *Science advances*, *4*(5),
523 eaat0661.

- 524 Gao, H., Schmidt, D. A., & Weldon, R. J. (2012). Scaling relationships of source pa-
 525 rameters for slow slip events. *Bulletin of the Seismological Society of America*,
 526 *102*(1), 352–360.
- 527 Ghosh, A., Vidale, J. E., Sweet, J. R., Creager, K. C., Wech, A. G., Houston, H.,
 528 & Brodsky, E. E. (2010). Rapid, continuous streaking of tremor in cascadia.
 529 *Geochemistry, Geophysics, Geosystems*, *11*(12).
- 530 Griffith, A. A. (1921). Vi. the phenomena of rupture and flow in solids. *Philosophi-
 531 cal transactions of the royal society of london. Series A, containing papers of a
 532 mathematical or physical character*, *221*(582-593), 163–198.
- 533 Hawthorne, & Bartlow, N. (2018). Observing and modeling the spectrum of a slow
 534 slip event. *Journal of Geophysical Research: Solid Earth*, *123*(5), 4243–4265.
- 535 Hawthorne, Bostock, M. G., Royer, A. A., & Thomas, A. M. (2016). Variations in
 536 slow slip moment rate associated with rapid tremor reversals in c ascadia. *Geo-
 537 chemistry, Geophysics, Geosystems*, *17*(12), 4899–4919.
- 538 Hawthorne, & Rubin, A. (2013a). Laterally propagating slow slip events in a rate
 539 and state friction model with a velocity-weakening to velocity-strengthening
 540 transition. *Journal of Geophysical Research: Solid Earth*, *118*(7), 3785–3808.
- 541 Hawthorne, & Rubin, A. M. (2013b). Tidal modulation and back-propagating
 542 fronts in slow slip events simulated with a velocity-weakening to velocity-
 543 strengthening friction law. *Journal of Geophysical Research: Solid Earth*,
 544 *118*(3), 1216–1239.
- 545 Heimisson, E. R. (2020). Crack to pulse transition and magnitude statistics dur-
 546 ing earthquake cycles on a self-similar rough fault. *Earth and Planetary Sci-
 547 ence Letters*, *537*, 116202.
- 548 Hicks, S. P., Okuwaki, R., Steinberg, A., Rychert, C. A., Harmon, N., Abercrombie,
 549 R. E., ... others (2020). Back-propagating supershear rupture in the 2016 mw
 550 7.1 romanche transform fault earthquake. *Nature Geoscience*, *13*(9), 647–653.
- 551 Houston, H., Delbridge, B. G., Wech, A. G., & Creager, K. C. (2011). Rapid tremor
 552 reversals in cascadia generated by a weakened plate interface. *Nature Geo-
 553 science*, *4*(6), 404–409.
- 554 Idini, B., & Ampuero, J.-P. (2020). Fault-zone damage promotes pulse-like rupture
 555 and back-propagating fronts via quasi-static effects. *Geophysical Research Let-
 556 ters*, *47*(23), e2020GL090736.
- 557 Ikari, M. J., & Saffer, D. M. (2011). Comparison of frictional strength and velocity
 558 dependence between fault zones in the nankai accretionary complex. *Geochem-
 559 istry, Geophysics, Geosystems*, *12*(4).
- 560 Im, K., Saffer, D., Marone, C., & Avouac, J.-P. (2020). Slip-rate-dependent friction
 561 as a universal mechanism for slow slip events. *Nature Geoscience*, *13*(10), 705–
 562 710.
- 563 Irwin, G. R. (1957). Analysis of stresses and strains near the end of a crack travers-
 564 ing a plate.
- 565 Jolivet, R., Candela, T., Lasserre, C., Renard, F., Klinger, Y., & Doin, M.-P. (2015).
 566 The burst-like behavior of aseismic slip on a rough fault: The creeping section
 567 of the haiyuan fault, china. *Bulletin of the Seismological Society of America*,
 568 *105*(1), 480–488.
- 569 Jolivet, R., & Frank, W. (2020). The transient and intermittent nature of slow slip.
 570 *AGU Advances*, *1*(1), e2019AV000126.
- 571 Kirkpatrick, J. D., Edwards, J. H., Verdecchia, A., Kluesner, J. W., Harrington,
 572 R. M., & Silver, E. A. (2020). Subduction megathrust heterogeneity character-
 573 ized from 3d seismic data. *Nature Geoscience*, *13*(5), 369–374.
- 574 Kirkpatrick, J. D., Fagereng, Å., & Shelly, D. R. (2021). Geological constraints on
 575 the mechanisms of slow earthquakes. *Nature Reviews Earth & Environment*,
 576 *2*(4), 285–301.
- 577 Lavier, L. L., Bennett, R. A., & Duddu, R. (2013). Creep events at the brittle duc-
 578 tile transition. *Geochemistry, Geophysics, Geosystems*, *14*(9), 3334–3351.

- 579 Lay, T., Kanamori, H., Ammon, C. J., Koper, K. D., Hutko, A. R., Ye, L., ... Rush-
580 ing, T. M. (2012). Depth-varying rupture properties of subduction zone
581 megathrust faults. *Journal of Geophysical Research: Solid Earth*, *117*(B4).
- 582 Liu, Y., & Rice, J. R. (2005). Aseismic slip transients emerge spontaneously in
583 three-dimensional rate and state modeling of subduction earthquake sequences.
584 *Journal of Geophysical Research: Solid Earth*, *110*(B8).
- 585 Liu, Y., & Rice, J. R. (2007). Spontaneous and triggered aseismic deformation
586 transients in a subduction fault model. *Journal of Geophysical Research: Solid*
587 *Earth*, *112*(B9).
- 588 Luo, Y., & Ampuero, J.-P. (2018). Stability of faults with heterogeneous friction
589 properties and effective normal stress. *Tectonophysics*, *733*, 257–272.
- 590 Luo, Y., & Liu, Z. (2021). Fault zone heterogeneities explain depth-dependent pat-
591 tern and evolution of slow earthquakes in cascadia. *Nature communications*,
592 *12*(1), 1–13.
- 593 Marone, C. (1998). Laboratory-derived friction laws and their application to seismic
594 faulting. *Annual Review of Earth and Planetary Sciences*, *26*(1), 643–696.
- 595 Michel, S., Gualandi, A., & Avouac, J.-P. (2019). Similar scaling laws for earth-
596 quakes and cascadia slow-slip events. *Nature*, *574*(7779), 522–526.
- 597 Nie, S., & Barbot, S. (2021). Seismogenic and tremorgenic slow slip near the sta-
598 bility transition of frictional sliding. *Earth and Planetary Science Letters*, *569*,
599 117037.
- 600 Obara, K., Hirose, H., Yamamizu, F., & Kasahara, K. (2004). Episodic slow slip
601 events accompanied by non-volcanic tremors in southwest japan subduction
602 zone. *Geophysical Research Letters*, *31*(23).
- 603 Obara, K., Matsuzawa, T., Tanaka, S., & Maeda, T. (2012). Depth-dependent mode
604 of tremor migration beneath kii peninsula, nankai subduction zone. *Geophys-
605 ical Research Letters*, *39*(10).
- 606 Peng, & Gombert, J. (2010). An integrated perspective of the continuum between
607 earthquakes and slow-slip phenomena. *Nature geoscience*, *3*(9), 599–607.
- 608 Peng, & Rubin, A. M. (2018). Simulating short-term evolution of slow slip influ-
609 enced by fault heterogeneities and tides. *Geophysical Research Letters*, *45*(19),
610 10–269.
- 611 Power, W., Tullis, T., Brown, S., Boitnott, G., & Scholz, C. (1987). Roughness of
612 natural fault surfaces. *Geophysical Research Letters*, *14*(1), 29–32.
- 613 Power, W. L., & Tullis, T. E. (1991). Euclidean and fractal models for the descrip-
614 tion of rock surface roughness. *Journal of Geophysical Research: Solid Earth*,
615 *96*(B1), 415–424.
- 616 Radiguet, M., Cotton, F., Vergnolle, M., Campillo, M., Valette, B., Kostoglodov, V.,
617 & Cotte, N. (2011). Spatial and temporal evolution of a long term slow slip
618 event: the 2006 guerrero slow slip event. *Geophysical Journal International*,
619 *184*(2), 816–828.
- 620 Renard, F., & Candela, T. (2017). Scaling of fault roughness and implications for
621 earthquake mechanics. *Fault zone dynamic processes: Evolution of fault proper-
622 ties during seismic rupture*, *227*, 197–216.
- 623 Rice, J. R. (1993). Spatio-temporal complexity of slip on a fault. *Journal of Geo-
624 physical Research: Solid Earth*, *98*(B6), 9885–9907.
- 625 Rogers, G., & Dragert, H. (2003). Episodic tremor and slip on the cascadia subduc-
626 tion zone: The chatter of silent slip. *Science*, *300*(5627), 1942–1943.
- 627 Romanet, P., Sato, D. S., & Ando, R. (2020). Curvature, a mechanical link between
628 the geometrical complexities of a fault: application to bends, kinks and rough
629 faults. *Geophysical Journal International*, *223*(1), 211–232.
- 630 Rousset, B., Fu, Y., Bartlow, N., & Bürgmann, R. (2019). Weeks-long and years-
631 long slow slip and tectonic tremor episodes on the south central alaska megath-
632 rust. *Journal of Geophysical Research: Solid Earth*, *124*(12), 13392–13403.

- 633 Rubin, A. M. (2008). Episodic slow slip events and rate-and-state friction. *Journal*
634 *of Geophysical Research: Solid Earth*, *113*(B11).
- 635 Rubin, A. M., & Ampuero, J.-P. (2005). Earthquake nucleation on (aging) rate and
636 state faults. *Journal of Geophysical Research: Solid Earth*, *110*(B11).
- 637 Ruina, A. (1983). Slip instability and state variable friction laws. *Journal of Geo-*
638 *physical Research: Solid Earth*, *88*(B12), 10359–10370.
- 639 Saffer, D. M., Frye, K. M., Marone, C., & Mair, K. (2001). Laboratory results indic-
640 ating complex and potentially unstable frictional behavior of smectite clay.
641 *Geophysical Research Letters*, *28*(12), 2297–2300.
- 642 Sagae, K., Nakahara, H., Nishimura, T., & Imanishi, K. (2023). Fine structure of
643 tremor migrations beneath the kii peninsula, southwest japan, extracted with
644 a space-time hough transform. *Journal of Geophysical Research: Solid Earth*,
645 *128*(6), e2022JB026248.
- 646 Segall, P., & Bradley, A. M. (2012). Slow-slip evolves into megathrust earthquakes in
647 2d numerical simulations. *Geophysical Research Letters*, *39*(18).
- 648 Segall, P., & Rice, J. R. (1995). Dilatancy, compaction, and slip instability of a
649 fluid-infiltrated fault. *Journal of Geophysical Research: Solid Earth*, *100*(B11),
650 22155–22171.
- 651 Segall, P., Rubin, A. M., Bradley, A. M., & Rice, J. R. (2010). Dilatant strengthen-
652 ing as a mechanism for slow slip events. *Journal of Geophysical Research: Solid*
653 *Earth*, *115*(B12).
- 654 Shelly, D. R., Beroza, G. C., & Ide, S. (2007). Complex evolution of transient slip
655 derived from precise tremor locations in western shikoku, japan. *Geochemistry,*
656 *Geophysics, Geosystems*, *8*(10).
- 657 Sun, Y., & Cattania, C. (2024, April). *Simulation Results in the Paper "Propaga-*
658 *tion of Slow Slip Events on Rough Faults: Clustering, Back Propagation, and*
659 *Re-rupturing" [Dataset]. Zenodo. Retrieved from [https://doi.org/10.5281/](https://doi.org/10.5281/zenodo.10988744)*
660 *zenodo.10988744* doi: 10.5281/zenodo.10988744
- 661 Tada, H., Paris, P. C., & Irwin, G. R. (1973). The stress analysis of cracks. *Hand-*
662 *book, Del Research Corporation*, *34*.
- 663 Wallace, L. M. (2020). Slow slip events in new zealand. *Annual Review of Earth and*
664 *Planetary Sciences*, *48*, 175–203.
- 665 Wech, A. G., & Bartlow, N. M. (2014). Slip rate and tremor genesis in cascadia.
666 *Geophysical Research Letters*, *41*(2), 392–398.
- 667 Yamashita, Yakiwara, H., Asano, Y., Shimizu, H., Uchida, K., Hirano, S., ... others
668 (2015). Migrating tremor off southern kyushu as evidence for slow slip of a
669 shallow subduction interface. *Science*, *348*(6235), 676–679.
- 670 Yamashita, S., Yagi, Y., & Okuwaki, R. (2022). Irregular rupture propagation
671 and geometric fault complexities during the 2010 mw 7.2 el mayor-cucapah
672 earthquake. *Scientific reports*, *12*(1), 1–10.
- 673 Yin, A. (2018). Water hammers tremors during plate convergence. *Geology*, *46*(12),
674 1031–1034.
- 675 Yin, A., Xie, Z., & Meng, L. (2018). A viscoplastic shear-zone model for deep (15–50
676 km) slow-slip events at plate convergent margins. *Earth and Planetary Science*
677 *Letters*, *491*, 81–94.

Abstract

Seismic and geodetic observations show that slow slip events (SSEs) in subduction zones can happen at all temporal and spatial scales and propagate at various velocities. Observation of rapid tremor reversals (RTRs) indicates back-propagating fronts traveling much faster than the main rupture front. Heterogeneity of fault properties, such as fault roughness, is a ubiquitous feature often invoked to explain this complex behavior, but how roughness affects SSEs is poorly understood. Here we use quasi-dynamic seismic cycle simulations to model SSEs on a rough fault, using normal stress perturbations as a proxy for roughness and assuming rate-and-state friction, with strengthening behavior at high slip rate. SSEs exhibit temporal clustering, large variations in rupture length and propagation speed, and back-propagating fronts at different scales. We identify a mechanism for back propagation: as ruptures propagate through low-normal stress regions, a rapid increase in slip velocity combined with rate-strengthening friction induces stress oscillations at the rupture tip, and the subsequent “delayed stress drop” induces secondary back-propagating fronts. Moreover, on rough faults with fractal elevation profiles, the transition from pulse to crack can also lead to the re-rupture of SSEs due to local variations in the level of heterogeneity. Our study provides a possible mechanism for the complex evolution of SSEs inferred from geophysical observations and its link to fault roughness.

Plain Language Summary

Aseismic slow slip events (SSEs), which like earthquakes can accommodate plate motions, are observed to happen intermittently, propagate backward, and travel at varying speeds. The rough geometry of faults causes heterogeneous stress distribution, which may be responsible for the complex slip behaviors. Here we use computer simulations and analytical tools to study the propagation of SSEs on rough faults. We find more small SSEs, occurring in short bursts, on a rougher fault. We also reproduce faster back-propagating streaks in simulations, analogous to seismological observations. On a fractal fault, ruptures can transition between slip modes (from inchworm-like to zipper-like) which further induces re-rupturing when propagating from high to low roughness areas. Our study helps quantify the effect of fault roughness and further understand underlying mechanics.

1 Introduction

Slow slip events are aseismic fault slip transients with a slip rate of about 1–100 mm/day (Wech & Bartlow, 2014; Hawthorne et al., 2016; Bletery et al., 2017; Frank et al., 2018; Bletery & Nocquet, 2020). Slow slip events (SSEs) and non-volcanic tremors have been observed worldwide in subduction zones, such as Cascadia, Nankai, and Hikurangi (Rogers & Dragert, 2003; Obara et al., 2004; Wallace, 2020). Several candidate mechanisms for slow slip events have been proposed, such as localized regions of lower normal stress (Liu & Rice, 2005, 2007; Rubin, 2008), fault gouge dilatancy (Segall & Rice, 1995; Segall et al., 2010), a transition to velocity-strengthening at a high slip rate (Hawthorne & Rubin, 2013a; Im et al., 2020), and frictional fault embedded within a viscous shear zone (Lavie et al., 2013; Yin et al., 2018; Behr et al., 2021).

Slow slip events exhibit remarkable spatio-temporal complexity. Frank (2016) and Frank et al. (2018) reveal smaller SSEs hidden within the interseismic periods and large events, respectively (also see Rousset et al. (2019)). They also find SSEs are clustered, similar to a cascade of aftershocks following the mainshock (Jolivet & Frank, 2020). Jolivet et al. (2015) and Hawthorne and Bartlow (2018) suggest that the moment of SSEs follows a power law distribution, which resembles Gutenberg-Richter law. The rupture style of SSEs, and the magnitude-duration scaling, are still subjects to debate. SSEs from different regions show a linear moment-duration scaling (Peng & Gombert, 2010; Gao et

63 al., 2012), associated with pulse-like rupture along an elongated fault (as inferred by Bartlow
 64 et al. (2011) and Radiguet et al. (2011)). On the other hand, events from a single region
 65 follow a duration-cubed scaling like earthquakes (Michel et al., 2019), reminiscent of crack-
 66 like propagation.

67 With advances in seismic and geodetic observations, uncommon slow slip behav-
 68 iors have been identified, and propagation velocities have been better measured. Wech
 69 and Bartlow (2014) use GPS measurement and locations of tremors to find that SSEs
 70 can rupture the same region again with a gap of about 3 weeks by bifurcating into bi-
 71 lateral propagation fronts in Cascadia. Yamashita et al. (2015) observe a re-rupturing
 72 event represented by migrating tremors several days after the first event in the Nankai
 73 subduction zone. Houston et al. (2011) and Obara et al. (2012) observed even faster back-
 74 propagating streaks represented by rapid tremor reversals (RTRs) in the Cascadia, and
 75 Nankai subduction zones, which have also been confirmed with borehole strainmeters (Hawthorne
 76 et al., 2016) and analysis of low-frequency earthquakes (Bletery et al., 2017).

77 These complex slip patterns are likely a manifestation of frictional behavior, fault
 78 heterogeneity, or the interplay between the two. As such, they offer an opportunity to
 79 understand the underlying physical mechanism for slow slip events and constrain fault
 80 properties in the environment of SSEs. Previous models incorporating heterogeneity typ-
 81 ically assume spatial variations in frictional properties: velocity weakening (VW) asper-
 82 ities embedded in a velocity strengthening (VS) fault, producing localized stick-slip be-
 83 havior on a creeping fault (e.g., Luo and Liu (2021)). Other studies employ a velocity-
 84 cutoff model with a transition from velocity weakening to velocity strengthening behav-
 85 ior with increasing slip rate and introduce heterogeneity by varying the cutoff-velocity
 86 (Peng & Rubin, 2018). While the existence of mixed-mode behavior at depths correspond-
 87 ing to SSEs is supported by observations (Behr & Bürgmann, 2021; Kirkpatrick et al.,
 88 2021), their spatial distribution is not well constrained, and modeling studies have ap-
 89 proximated them by placing asperities at random locations, or on a grid (Peng & Ru-
 90 bin, 2018; Luo & Ampuero, 2018). Additionally, several mechanisms have been proposed
 91 to explain back propagation and rapid tremor reversals, such as tidal modulation (Hawthorne
 92 & Rubin, 2013b), fluid pressure wave (Cruz-Atienza et al., 2018; Yin, 2018), fault het-
 93 erogeneity (Luo & Ampuero, 2018; Luo & Liu, 2021), and fault damage zone (Idini &
 94 Ampuero, 2020).

95 Fault roughness represents a ubiquitous and well-characterized source of hetero-
 96 geneity, and like other heterogeneities described above, it can modulate fault stability
 97 (Cattania & Segall, 2021). The migrations of tremors in the Nankai subduction zone ex-
 98 hibit spatial variations of predominant directions (either along strike or dip), as shown
 99 in Sagae et al. (2023). This implies that structural heterogeneities, like fault roughness,
 100 play a significant role due to their known anisotropic properties (Renard & Candela, 2017),
 101 rather than just material differences. Furthermore, it is well established that fault rough-
 102 ness controls the spatial distribution of fault normal stresses (Fang & Dunham, 2013;
 103 Romanet et al., 2020; Cattania & Segall, 2021), and the effect of normal stress pertur-
 104 bations depends on the ratio of normal stress perturbations to background effective nor-
 105 mal stress. Due to the low normal stress conditions associated with SSEs, the change
 106 of normal stress due to fault roughness may play an important role in controlling their
 107 behavior, making them an ideal setting in which to study the effect of heterogeneity on
 108 fault slip patterns. In this study, we seek to determine the effect of fault roughness on
 109 the complex rupture behaviors during SSEs. We use numerical simulations and fracture
 110 mechanics to address the following question: Can fault roughness explain the spatio-temporal
 111 variety of SSE behavior, back propagation, and re-rupture?

112 After introducing the modeling framework (Section 2), we consider the simple case
 113 of sinusoidal perturbations in normal stress (Section 3.1) and show that heterogeneity
 114 with small wavelength and large amplitudes favors complex slip behaviors including a
 115 variety of rupture dimension, clustering, and forward and backward, fast and slow prop-

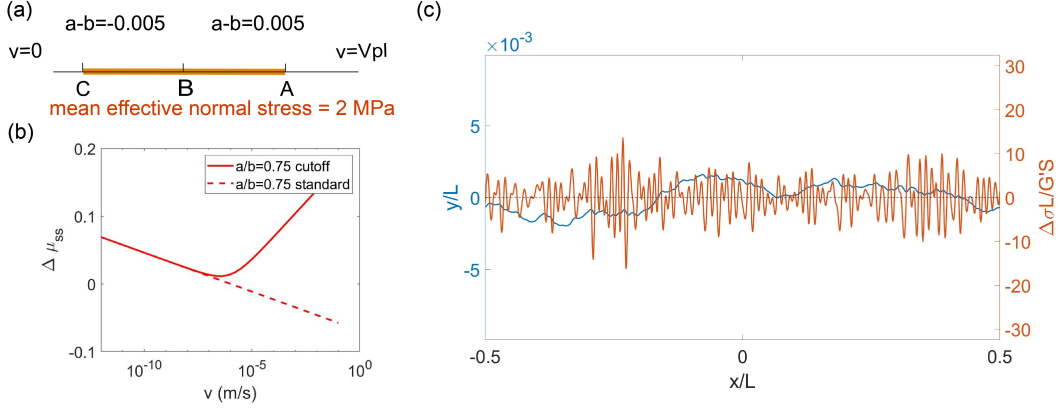


Figure 1. (a) Model geometry. (b) The steady-state friction coefficient of the original rate-and-state friction (dashed line) and velocity cutoff model (solid line, Equation 2). (c) An example of normalized elevation of a rough fault y/L (blue) and perturbation of the normal stress per slip $\Delta \sigma L/G'S$ (red) obtained from Equation 4.

116 agation. Furthermore, we introduce an analytical tool based on fracture mechanics to
 117 explain why SSEs arrest or propagate on a fault with variable normal stress. In Section 3.2,
 118 we discuss a possible mechanism to generate fast-moving back-propagating fronts: a de-
 119 layed stress drop induced by the coupling between normal stress heterogeneity and fric-
 120 tion. Finally, in Section 3.3 we consider a fractal fault, and demonstrate that its irreg-
 121 ular distribution of normal stresses produces dynamics that are not captured by the si-
 122 nusoidal model. In particular, we demonstrate SSE re-rupturing can be induced by a tran-
 123 sition between the pulse to crack-like rupture, as the rupture propagates through regions
 124 of variable local roughness amplitude.

125 2 Models

126 We use the 2D quasi-dynamic boundary element model FDRA (Segall & Bradley,
 127 2012) to simulate SSE cycles on a rough fault. We include normal stress perturbations
 128 as proxies for roughness due to its lower computation cost. The evolution of normal stress
 129 and fault geometry is not considered in this study. Thus, our simulations can be thought
 130 as freeze-frame in the tectonic time scale. This simplification is justified because normal
 131 stress perturbations grow linearly with slip, and a single SSE only increases the total slip
 132 by a small fraction, so that normal stress perturbations do not change significantly dur-
 133 ing several cycles.

134 The model consists of an in-plane fault (mode II) in full space with velocity bound-
 135 ary conditions of tectonic loading rate v_{pl} and 0 at A and C, respectively (Figure 1a; Ta-
 136 ble 1), representing the region between the locked seismogenic zone and steady creep,
 137 where deep SSEs have been observed (Obara et al., 2004; Rogers & Dragert, 2003; Lay
 138 et al., 2012). The fault is composed of a shallow seismogenic (velocity-weakening) region,
 139 BC, and a deep creeping (velocity-strengthening) region, AB. Fault slip is governed by:

$$\tau_{el} = \tau_f + \frac{G}{2c_s}v, \quad (1)$$

140 where τ_{el} is the shear stress due to remote loading and interaction between elements, τ_f
 141 is the frictional resistance, and $\frac{G}{2c_s}v$ is the radiation damping term with shear wave ve-
 142 locity c_s and shear modulus G (Rice, 1993). Slow slip events on a velocity weakening
 143 require a stabilizing mechanism, such a reduction in pore pressure due to slip-induced

Table 1. Model parameters

parameter	value
fault length L	2.5 or 10 km
tectonic loading rate v_{pl}	1×10^{-9} m/s
shear modulus G	3×10^{10} Pa
Poisson's ratio ν	0.25
S wave velocity c_s	3.7×10^3 m/s
friction coefficient μ_0	0.6
reference slip rate v^*	1×10^{-6} m/s
cut-off slip rate v_c	1×10^{-6} m/s
slip rate $v_{\tau-min}$ with minimum steady-state friction	3.33×10^{-7} m/s
friction parameter a for velocity-weakening region	0.015
friction parameter a for velocity-strengthening region	0.025
friction parameter b	0.02
characteristic slip distance D_c	4×10^{-5} m
average normal stress σ_0	2 MPa
amplitude-to-wavelength ratio α_r	0.001
Hurst exponent H	0.7

144 dilatancy (Segall & Rice, 1995) or a transition to velocity strengthening friction with in-
 145 creasing slip velocity, demonstrated in laboratory experiments (Saffer et al., 2001; Ikari
 146 & Saffer, 2011). Here we assume the latter mechanism and employ the velocity-cutoff
 147 model introduced by Hawthorne and Rubin (2013a). Frictional resistance is given by:

$$\tau_f = \left[\mu_1 + a \ln \frac{v}{v^*} + b \ln \left(\frac{\theta v_c}{D_c} + 1 \right) \right] \sigma, \quad (2)$$

148 where $\sigma, \mu_1, v, v^*, \theta, D_c$ and v_c represent normal stress, reference frictional coefficient, slip
 149 rate, reference slip rate, state variable, characteristic slip distance, and cutoff velocity,
 150 respectively. a and b are the coefficients for instant and evolution effects. State evolu-
 151 tion is governed by the aging law (Ruina, 1983) as:

$$\dot{\theta} = 1 - \frac{\theta v}{D_c}. \quad (3)$$

152 In contrast, the original rate-and-state friction is $\mu = \mu_0 + a \ln \frac{v}{v^*} + b \ln \frac{\theta v^*}{D_c}$. To match
 153 two frictional laws at low slip rate, we set μ_1 as $\mu_0 + b \ln \frac{v^*}{v_c}$ (Equation 2). As shown in
 154 Figure 1b, the steady-state friction $\mu_{ss} = \mu_1 + a \ln \frac{v}{v^*} + b \ln \left(\frac{v^*}{v} + 1 \right)$ decreases to a mini-
 155 mum when v reaches $v_{\tau-min} = \frac{b-a}{a} v_c$, and then increases with increasing slip rate, so
 156 that slip instability initiates at $v < v_{\tau-min}$ and does not accelerate into an earthquake
 157 (Figure 1b).

158 The friction parameters a, b, D_c and average normal stress σ_0 we use are shown in
 159 Table 1 and consistent with previous studies (Marone, 1998; Liu & Rice, 2007; Audet
 160 & Kim, 2016). The mean normal stress σ_0 used in the simulations is 2 MPa, which makes
 161 the stress drop $\Delta\tau_{drop}$ about 0.1 MPa, within the range of 0.01 to 1 MPa, consistent with
 162 those inferred by Gao et al. (2012). We impose a perturbation of normal stress, which
 163 mimics the stress heterogeneity on a rough fault with a constant wavelength or a frac-
 164 tal distribution (e.g. Figure 1c). We refer to patches of elevated normal stress as asper-
 165 ities throughout the paper. We set the minimum grid spacing to $\frac{1}{2.5}$ of the smallest co-
 166 hesive zone size L_c to adequately resolve the stress field across the crack tip (Erickson
 167 et al., 2023). The size of cohesive zone L_c is estimated as $1.377 \frac{G' D_c}{b \sigma_{max}^{1-\nu}}$ (Rubin & Ampuero,
 168 2005), where σ_{max} and G' are the maximum normal stress and $\frac{G'}{1-\nu}$, respectively.

169 We use synthetic fractal fault profiles, comparable to natural faults. Faults are cor-
 170 rugated at all scales, and the distribution is self-affine with a Hurst exponent H between
 171 0.4–0.8 (W. Power et al., 1987; Candela et al., 2012; Brodsky et al., 2016; Renard &
 172 Candela, 2017). The fractal fault topography has a power spectrum P^2 proportional to
 173 $(2\pi\lambda)^{-2H-1}$, where λ is the wavelength, and the root-mean-square elevation is given by
 174 $y_{RMS} = \alpha_r \lambda_{max}^H$, where α_r is the amplitude-to-wavelength ratio and λ_{max} is the max-
 175 imum wavelength. For instance, Figure 1c shows a fractal fault with a normalized wave-
 176 length λ/L from 0.01 to 1 and $\alpha_r = 0.001$. We use the following analytical expressions
 177 to relate normal stress perturbations to fault topography (Fang & Dunham, 2013; Cat-
 178 tania & Segall, 2021):

$$\Delta\sigma(x) = \frac{G'S}{2} \mathcal{H}(y'') = \frac{G'S}{2} \int_{-\infty}^{\infty} \frac{y''(\xi)}{x-\xi} d\xi, \quad (4)$$

179 where S is the total slip, and additional shear stress is given by $\Delta\tau(x) = \frac{G'S}{2} y' \mathcal{H}(y'')$,
 180 where $\mathcal{H}(y'')$ is the Hilbert transform of the second derivative of the elevation ampli-
 181 tude y , and S is the accumulated slip. This formula describes $\Delta\sigma$ increases linearly with
 182 S in the elastic regime and does not apply when S is large enough to cause plastic de-
 183 formation or fracturing. The corrugation perturbs the normal stress and shear stress lo-
 184 cally at the scale of the smallest wavelength λ_{min} (Fang & Dunham, 2013; Romanet et
 185 al., 2020; Cattania & Segall, 2021). The root-mean-square (RMS) of normal stress per-
 186 turbation is $\Delta\sigma_{RMS} = (2\pi)^2 \alpha_r \sqrt{\frac{H}{2-H} \frac{G'S}{2} \lambda_{min}^{H-2}}$. While the mean of $\Delta\tau$ is $\Delta\tau_{mean} =$
 187 $(2\pi)^3 \alpha_r^2 \frac{2H}{3-2H} \frac{G'S}{2} \lambda_{min}^{2H-3}$, which is proportional to α_r^2 while $\Delta\sigma_{RMS}$ is proportional to α_r .
 188 The amplitude-to-wavelength ratio α_r of natural faults is about 10^{-3} to 10^{-2} (W. L. Power
 189 & Tullis, 1991). Therefore, we only consider the roughness-induced normal stress per-
 190 turbation $\Delta\sigma$ but not the shear stress $\Delta\tau$ because it is much smaller than $\Delta\sigma$. We use
 191 a slip rate threshold to identify SSEs and to estimate propagation velocities for individ-
 192 ual ruptures and cascading clusters (more detail is provided in section Appendix A).

193 3 Results

194 To obtain insight into how roughness affects slow slip behavior, we first explore the
 195 simple case of sinusoidal perturbations with varying wavelengths and amplitudes; in Sec-
 196 tion 3.3 we consider the more realistic case of normal stresses induced by slip on a frac-
 197 tal fault.

198 3.1 Variety of slip behavior on a sinusoidal rough fault

199 We consider a rough fault with a sinusoidal normal stress distribution with a mag-
 200 nitude given by

$$\sigma(x) = \sigma_0 + \sigma_A \cos \frac{2\pi x}{\lambda}. \quad (5)$$

201 Simulations exhibit a range of SSE behaviors, varying with both wavelength λ and am-
 202 plitude of the normal stress perturbation σ_A . Figure 2 shows a slip behavior as a func-
 203 tion of λ and σ_A/σ_0 . To better highlight differences between simulations, we plot accu-
 204 mulated slip normalized by the theoretical slip profile or a crack driven by end-point dis-
 205 placement (in this case provided by deep creep), given by Rubin (2008):

$$S(x, t) = \frac{S(L, t)}{\pi} \left(\frac{\pi}{2} + \arcsin \frac{x - L/2}{L/2} \right), \quad (6)$$

206 where L , x , and t are the fault length, the location on the fault, and time. We choose
 207 a 2.5 km-long flat fault that is a few times larger than the nucleation length, so that it
 208 only has full ruptures in the homogeneous- σ case (see Cattania (2019)), as shown in Fig-
 209 ure 2a and 2b. In this case, full ruptures are well approximated as a constant stress drop
 210 crack (Figure 2a), with an elliptical slip profile (Eshelby, 1957). Cases with low σ_A/σ_0

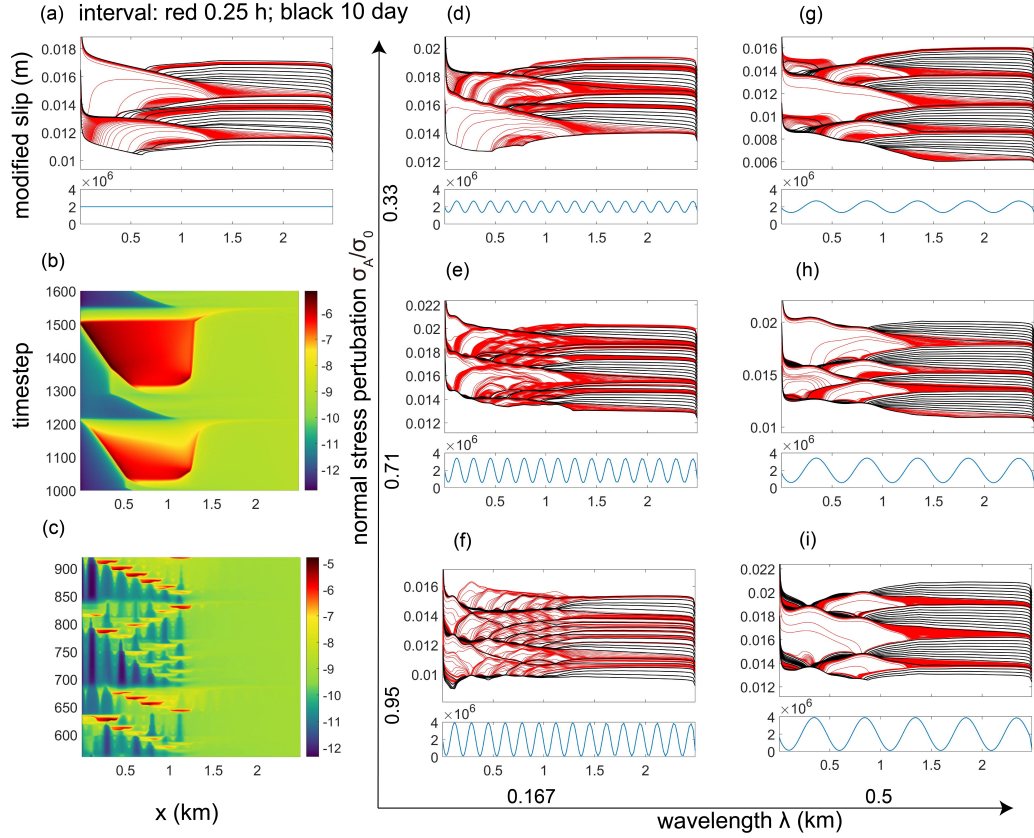


Figure 2. Effect of sinusoidal normal stress perturbations on rupture style. (a) normalized slips with uniform σ . Normalized slip equals slip s divided by $\frac{\pi}{2} + \arcsin \frac{x-W/2}{W/2}$. (d-i) Normalized slip profiles as a function of wavelength (λ) and perturbation amplitude (σ_A/σ_0). (b) and (c) show the slip rate for each time step for cases (a) and (f), respectively.

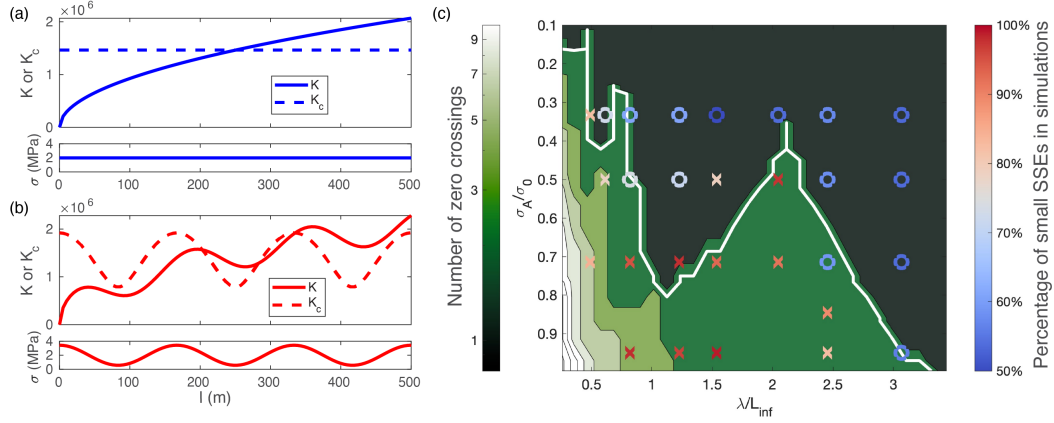


Figure 3. Stress intensity factor K (solid line) and local toughness K_c (dashed line) for the constant (a) and perturbed (b) normal stress. The slip will arrest at $l = 280$ m. (c) Number of zero crossings of $K - K_c$ and percentage of small SSEs in simulations with varying normalized wavelength λ/L_∞ and amplitude-to-constant ratio σ_A/σ_0 . The red contouring line represents the threshold for arresting (3 zero crossings). Colors of circles and crosses represent the percentage of events smaller than 2λ in the simulations with a 2.5 km-long fault (circle: > 0.75 ; cross: < 0.75).

211 and long wavelength exhibit crack-like ruptures and partial ruptures (Figure 2d, 2g and
 212 2h), whereas with the increase of wavenumber and perturbation amplitude σ_A , there are
 213 more pulse-like ruptures composed of localized slip pockets and an overall flat slip pro-
 214 file (Figure 2f). A similar transition from crack to pulse-like rupture due to fault rough-
 215 ness was observed by Heimisson (2020), and interpreted as a consequence of additional
 216 shear resistance from fault roughness (roughness drag; Fang and Dunham (2013)). Our
 217 results indicate that pulse-like rupture can still occur exclusively as a result of a pertur-
 218 bation in normal stress. Each cluster ruptures the whole velocity-weakening region inter-
 219 mittently, and it ruptures more than once in some regions (Figure 2c and 2f). Note
 220 that these partial ruptures are often nucleated at a high- σ region and arrested by the
 221 high- σ regions nearby (Figure 2f and 2i), which have a higher local fracture energy, as
 222 discussed below.

223 3.1.1 Rupture arrest with variable normal stress

224 To get more insight into rupture arrest, we use a fracture mechanics criterion ac-
 225 counting for heterogeneity. Rupture propagation is controlled by the criterion: $K = K_c$,
 226 where K and K_c are stress intensity factor and local toughness, respectively (Griffith,
 227 1921; Irwin, 1957). Normal stress heterogeneity affects both these terms: enhanced com-
 228 pression at the crack tip increases the local toughness K_c , thus favoring rupture arrest;
 229 however, it also increases the stress drop and hence K , which promotes rupture prop-
 230 agation. Analytical calculations are described in Appendix B.

231 Figure 3a and b illustrate examples of K and K_c distributions for constant and per-
 232 turbed normal stress. The zero crossing of $K - K_c$ of a smooth fault (red) is located
 233 at about $l \approx 250$ m, which is similar to the nucleation half length $L_\infty = \frac{G' b D_c}{\pi (b-a)^2 \sigma}$. As
 234 the crack reaches the nucleation dimension, it will grow unstable and propagate indef-
 235 initely as long as the stress drop remains uniform. However, $K - K_c$ has 3 zero cross-
 236 ings for the case with perturbed normal stress (blue). The SSE is likely to nucleate at
 237 the first zero crossing ($l \approx 200$ m) and arrest at the second zero crossing ($l \approx 280$ m)
 238 because it cannot penetrate the high- σ region ($l \approx 280 - 330$ m) where $K < K_c$.

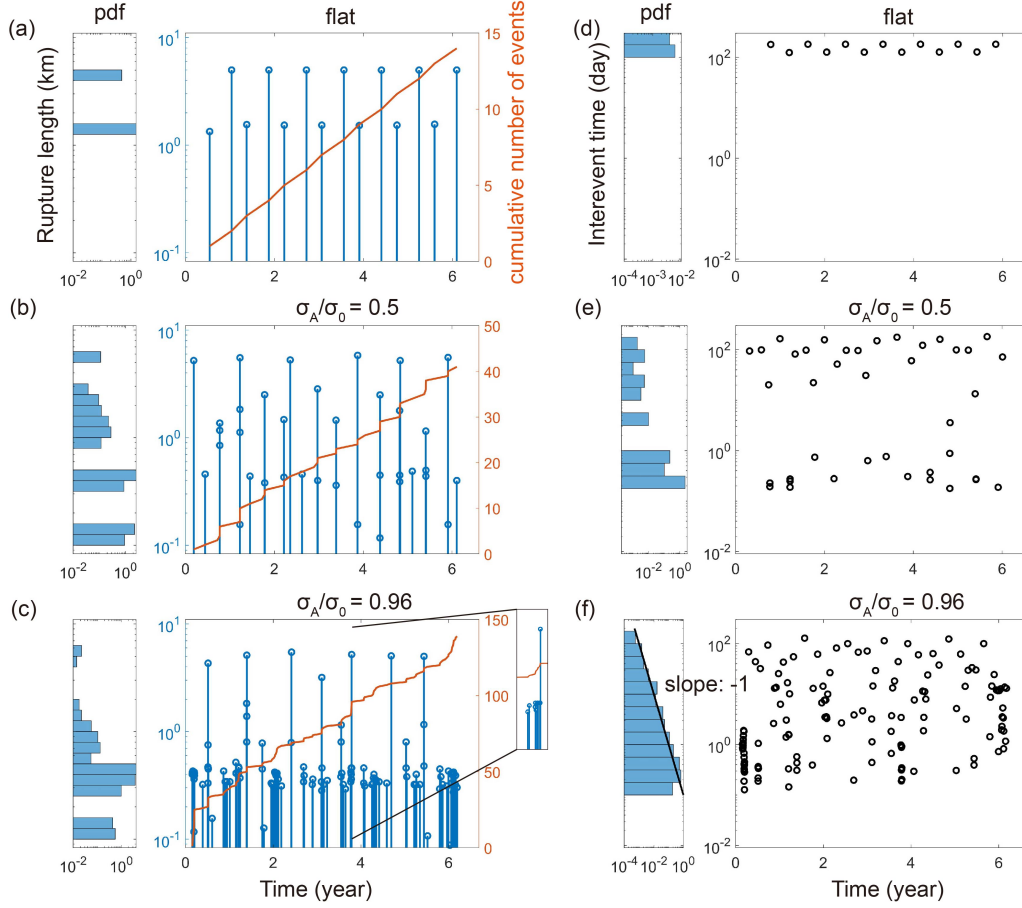


Figure 4. Effect of perturbation amplitude on SSE catalogs. Rupture lengths (a, b, c) and interevent times (d, e, f) with increasing sinusoidal σ perturbation on a 10 km-long fault ($\lambda = 0.33$ km). SSEs are outlined by a threshold of 1×10^{-6} m/s. Events that are closer than the duration of full ruptures are merged as one.

239 Figure 3c shows the conditions under which SSEs might arrest according to this
 240 analysis. Figure 3c excludes the perturbed wavelength shorter than the cohesive zone
 241 ($1.377L_b \approx 55$ m), with $L_b = \frac{G'D_c}{b\sigma}$ (Rubin & Ampuero, 2005; Ampuero & Rubin, 2008),
 242 because local toughness K_c cannot be calculated as Equation B4 due to the varying normal
 243 stress in the cohesive zone. If $K - K_c$ has more than three zero crossings in Figure 3b,
 244 the SSEs tend to stop at the high-normal-stress region and propagate like a pulse
 245 discontinuously. Therefore, the parameter space for arresting is below the white curve,
 246 while the black area indicates that ruptures will not arrest. For the same wavelength λ ,
 247 SSEs are more likely to arrest if the normal stress perturbation is larger. The range of
 248 wavelength promoting rupture arrest is narrow for smaller normal stress perturbations.
 249 We also compare our analytical model with the percentage of SSEs smaller than 2λ
 250 in the simulations (several cases are shown in Figure 2) since there are more small SSEs
 251 if arresting happens more frequently. The cross indicates that most SSEs ($> 75\%$) are
 252 small, while the circle indicates fewer small ruptures ($< 75\%$). To first order, the dis-
 253 tribution of crosses and circles shows a Z-shaped boundary and our model aligns with
 254 simulations. This analysis demonstrates that the strong spatial variations of both local
 255 toughness K_c and stress intensity factor K of potential ruptures along the rough fault
 256 can account for the breakdown of a single large SSE into multiple smaller SSEs.

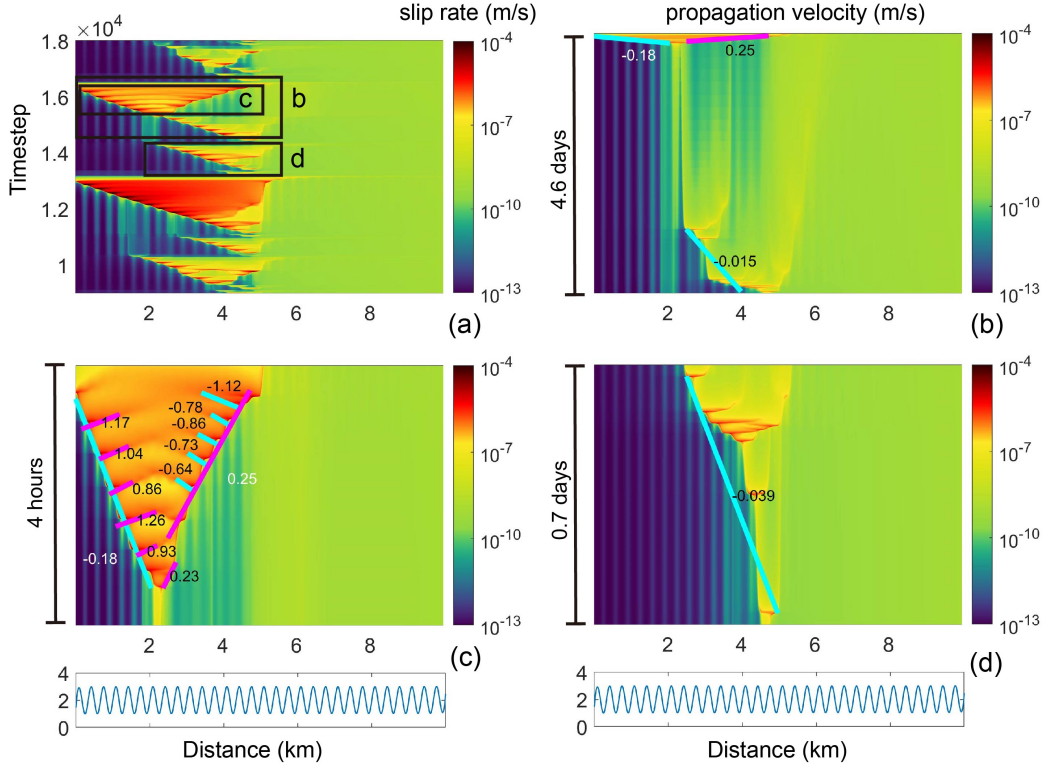


Figure 5. Evolution of SSE cycles (a), consisting of pre-slips plus full rupture (b), full rupture with back-propagating fronts (c) and clustered subevents (d) and normal stress distribution with $\lambda = 0.33$ km and $\sigma_A/\sigma_0 = 0.5$. The fitting lines for updip and downdip propagation are in light blue and pink respectively and the corresponding velocity is noted beside (unit: m/s). The threshold slip rate for outlining events is 1×10^{-6} m/s.

257

3.1.2 Temporal statistics and size distribution

258

259

260

261

262

263

264

265

266

267

268

269

270

271

272

273

The SSE catalogs simulated on a fault with higher roughness show more randomness and clustering (Figure 4). Figure 4a and d exhibit stable SSE cycles consisting of a full rupture and a partial rupture on a 10 km-long flat fault. However, for the rough fault, Figure 4b and c shows a larger number of SSEs with increasing amplitude of σ perturbations, consistent with the analysis in the previous section. The SSE interevent time catalog for the case with $\sigma_A/\sigma_0 = 0.5$ shows two groups of intervals of about 100 days and 1 hour (Figure 4b), corresponding to the time between full rupture and subsequent cluster, and the time between subevents within pre-slip and subsequent clusters, respectively. However, the case with a higher $\sigma_A/\sigma_0 = 0.96$ exhibits more continuously distributed intervals spanning four orders of magnitude, from 10 minutes to 100 days (Figure 4c), with temporal clustering around the largest events. More small SSEs also appear on faults with higher roughness (Figure 4e and 4f). A cluster of small events can cause less uniform background stress, so the rupture length and time for the next event are less predictable. This result is similar to the observations showing that a large SSE can be decomposed into a cluster of smaller events (Jolivet et al., 2015; Frank, 2016; Frank et al., 2018; Rousset et al., 2019; Jolivet & Frank, 2020).

274

3.1.3 Rupture velocities

275

276

277

278

279

280

281

282

283

284

285

286

287

Fault roughness also promotes a range of propagation directions and velocities. Figure 5a shows that one SSE cycle on a rough fault is composed of a cluster of pre-slips (Figure 5b), full rupture (Figure 5c) and clustered subevents (Figure 5d). The dimension of subevents is one to several wavelengths, and they are confined by asperities. The clusters usually start from the boundary of the seismogenic and creeping regions and generally propagate updip intermittently, but sometimes propagate downdip (Figure 5b and 5d). Full ruptures usually nucleate at the end of the cluster of pre-slips (Figure 5b). The updip and downdip propagations of full ruptures exhibit similar velocities: 0.18 and 0.25 m/s (15.5 and 21.6 km/day). However, the propagation velocities of the pre-slip cluster and the subsequent events are smaller than that of the full rupture by a factor of 5–10. This smaller velocity can be explained by the lower state variable θ : in the cluster of pre-slips and subsequent events, the event in the front is not triggered immediately because it is still below steady-state after the stress change.

288

3.2 Back propagating fronts

289

290

291

292

293

A common feature in rough fault simulations is the occurrence of fast back-propagating fronts within a full rupture (Figure 5c). Their propagation velocity is 3–7 times higher than the forward propagation. These secondary ruptures may be analogous to rapid tremor reversals (Houston et al., 2011) or fast streaks observed along dip (Shelly et al., 2007; Ghosh et al., 2010).

294

295

296

297

298

299

300

301

302

303

304

305

306

307

308

309

310

311

312

To understand the origin of back-propagating fronts, in Fig. 6 we compare the evolution of stress and slip velocities on flat and rough faults. On a smooth fault, the crack tip stress and velocity profiles are simply translated as the rupture propagates, and a constant stress drop within the rupture drives the crack at constant velocity (Figure 6a). On the other hand, propagation along rough faults induces large fluctuations in slip velocity and stress drop: the missing piece of the puzzle is a temporary positive stress change $\Delta\tau$ behind the crack tip, that enables ruptured asperities to break again and trigger a secondary slip front. We use the term “delayed stress drop” to describe this mechanism for back-propagating fronts on rough faults, which can be understood in the framework of rate-and-state friction law and velocity-cutoff model. In the case of forward propagation at the crack-tip, the slip rate in the low- σ region is significantly higher than that in the high- σ region (Figure 6d). When the rupture front passes the low- σ region, the slip rate on the asperity behind is also elevated to a similar level as the low- σ region (profile 3 in Figure 6d), which causes the shear stress to increase due to velocity-strengthening behavior at higher slip rate (Figure 1b, profile 3 in Figure 6c). As the rupture propagates into high σ regions, the slip velocity and stress decrease, as shown by the difference between stress profiles 4 and 3 (solid black line in Figure 6c). This delayed stress drop causes a stress increase on the asperities behind ($x \approx 800$ m and $x \approx 1300$ m), and hence induce secondary back propagation in its wave.

313

3.3 Pulse-to-crack transition and re-rupture on fractal faults

314

315

316

317

318

319

320

321

322

On a fractal fault, heterogeneity varies more randomly than in the sinusoidal cases presented above: since the local amplitude and (to a lesser extent) frequency content varies spatially, the slip regimes displayed in Figure 2 can all coexist on a single fault surface, and slip front propagation across these different regimes generates additional complexity. Figure 7 shows a case with a fractal rough fault with wavelength λ between 0.125 and 10 km and Hurst exponent $H = 0.7$. Within a single full rupture (about one day long), there are two kinds of rupture behaviors, first pulse-like and then crack-like. Additionally, some even faster “streaks” propagate backward in the simulations, analogous to be behavior discussed in section 3.2.

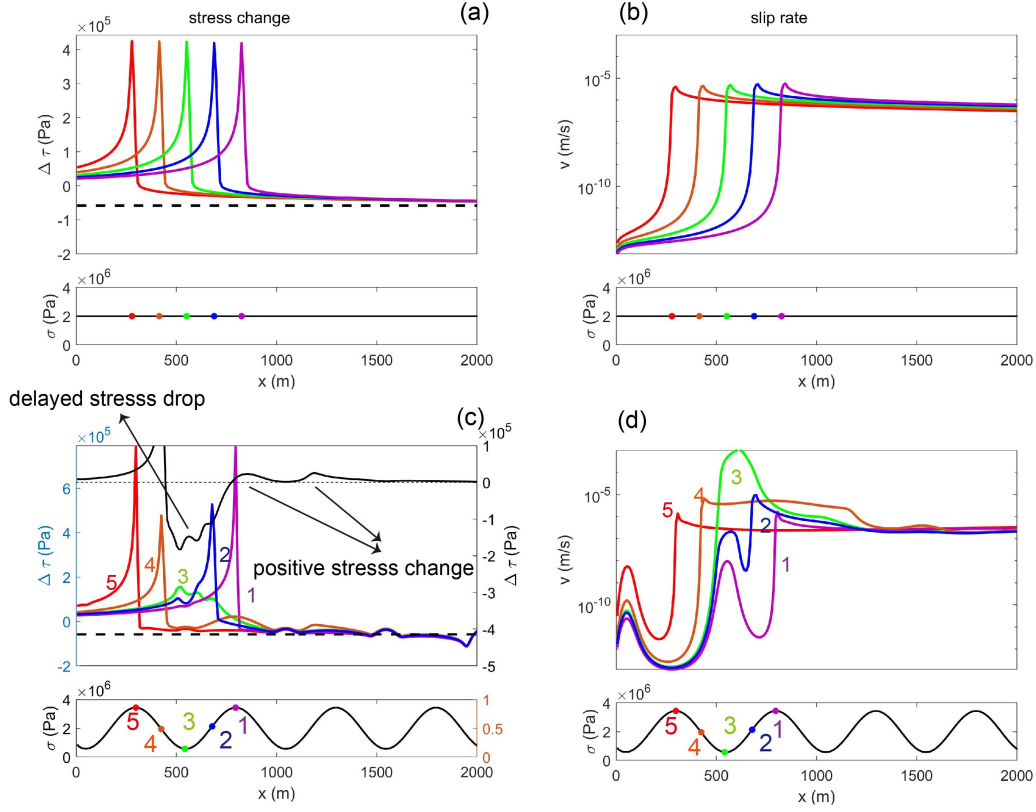


Figure 6. Stress change and slip rate profile along a flat fault (a and b) or fault with sinusoidal normal stress (c and d; $\lambda = 0.5$ km and $\sigma_A/\sigma_0 = 0.71$) when the rupture propagates from right to left. Colored lines represent profiles when the crack tips are at the extrema and mean of σ (c and d; coded by 1 to 5). The black line in (c) represents the difference between stress profiles 4 and 3. The dashed line represents the stress change after an event.

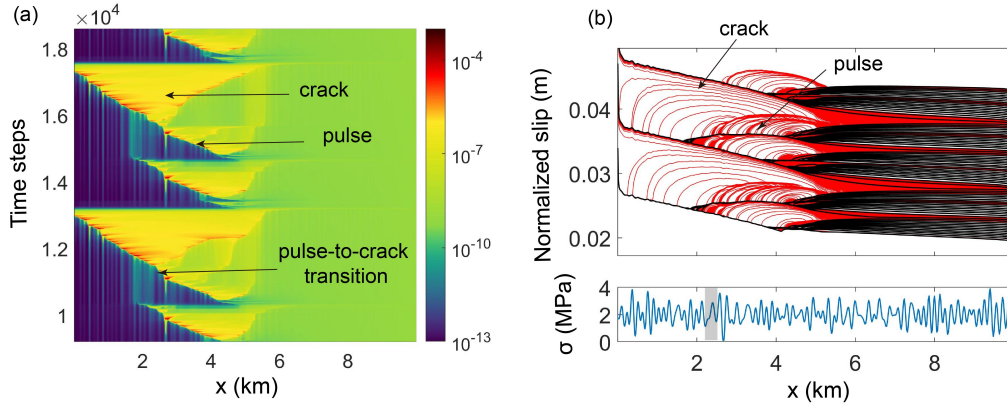


Figure 7. Slip behaviors on a fractal fault. (a) Slip rate across two SSE cycles. (b) Top: normalized slip along the fault during several SSE cycles, (cumulative slip divided by $\frac{\pi}{2} + \arcsin \frac{x-W/2}{W/2}$). The black lines represent interseismic slip with an interval of around 10 days. Red lines are plotted with an interval of 0.25 hour when the maximum slip rate is larger than v_{pl} . Bottom: distribution of the normal stress obtained from Equation 4 with $S = 55$ mm. The grey box denotes where the pulse-to-crack transition happens.

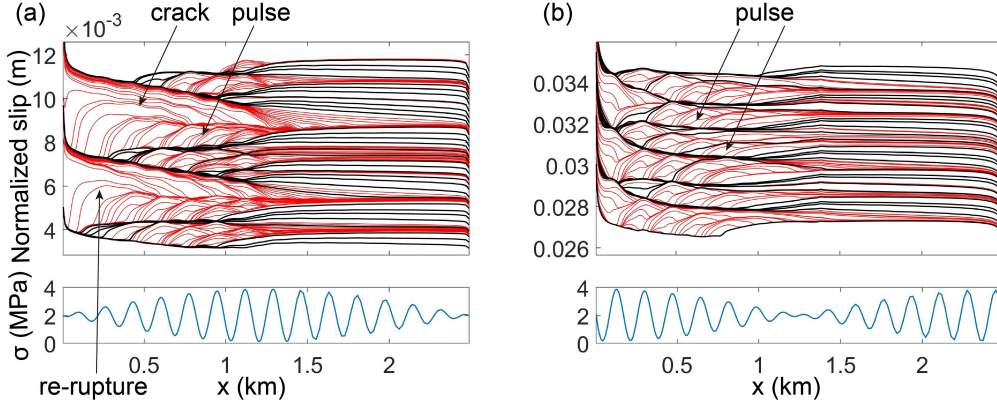


Figure 8. Normalized slip and normal stress for “walnut” case (a) and “hourglass” (b). (a) Re-rupture within a full-rupture event which propagates from high to low roughness regions. (b) SSEs propagating as a pulse from low to high roughness regions without re-rupture.

323 In Figure 7, pulse-like ruptures are usually clusters of small sub-events and propa-
 324 gate slowly, while crack-like ones are single extensive events and propagate much faster.
 325 As shown in section 3.1 and Figure 2, the amplitude of normal stress perturbations deter-
 326 mines whether a rupture propagates as a crack or a pulse. Therefore, we proposed that
 327 the transition from pulse to crack is caused by spatial variations of normal stress: higher
 328 amplitudes of normal stress perturbations favor pulse-like ruptures, so pulse-to-crack tran-
 329 sitions can take place as rupture propagates into regions with lower local roughness.

330 To test this, we compare two end-member cases of a “walnut” and an “hourglass”
 331 normal stress perturbation (Figure 8) to study how the local amplitude of the pertur-
 332 bation affects rupture propagation. We construct the normal stress perturbation with
 333 two sinusoidal functions of similar wavelengths, $0.179 \left(\frac{2.5}{14}\right)$ and $0.167 \left(\frac{2.5}{15}\right)$ km, with a
 334 group wavelength of 2.5 km. We find that day-long single events exhibit the pulse-to-
 335 crack transition and re-rupture in the “walnut” case (Figure 8a), in which the SSE propa-
 336 gates from high roughness to low roughness areas. Ruptures initiate as pulses in the
 337 region with a larger perturbation amplitude ($x \approx 1.25$ km) and evolve into cracks in
 338 the region with nearly constant normal stress ($x \approx 0$ km). We interpret this as caused
 339 by the deficit between crack and pulse-like slip profiles, a mechanism that was previously
 340 identified by Idini and Ampuero (2020) for faults surrounded by a damage zone. In prin-
 341 ciple, the slip deficit could also be filled with subsequent small SSEs as shown in Fig-
 342 ure 8b. We suggest that it is also easier for the re-rupture to penetrate the lower-roughness
 343 region ($x \approx 0$ km) due to absence of strong asperities, so that a single full rupture is
 344 favored. In contrast, ruptures remain pulse-like when propagating from the low into the
 345 high roughness region in the “hourglass” case (Figure 8b), which usually last on the or-
 346 der of 10 days. The presence of high normal stress (asperities) in the high roughness re-
 347 gion ($x \approx 0$ km) also prevents this area from re-rupturing in a single events, as Figure
 348 8a.

349 4 Discussion

350 In this study, we analyze how heterogeneous normal stress induced by fault rough-
 351 ness produces rich slip behavior during slow slip events. We reproduce SSEs with a range
 352 of rupture lengths on rough faults in the simulations, which is consistent with geodetic
 353 observations that show a power-law distribution of the sizes of slip bursts on a rough fault
 354 (Jolivet et al., 2015; Hawthorne & Bartlow, 2018), and is similar to an emerging cascade

355 of slow slips and foreshocks on rough faults from numerical simulations (Cattania & Segall,
 356 2021). Our simulations also exhibit clustering behaviors that a long-period SSE can be
 357 decomposed into several short subevents, which is analogous to the observations such
 358 as Frank et al. (2018) and Rousset et al. (2019). We suggest that fault roughness, a uni-
 359 versal characteristic in nature, can explain many complex dynamics of SSEs. This com-
 360 plexity can be simply understood within the context of linear elastic fracture mechan-
 361 ics.

362 Simulations show complex rupture behaviors on rough faults, including forward and
 363 back propagation at varying speeds, which differ from that on flat and frictionally uni-
 364 form faults. We observe strongly-varying slip rates when the rupture front first passes
 365 low and high normal stress regions, in contrast to roughly constant slip rate behind back-
 366 propagating fronts. The difference can be explained by initial conditions (state variable
 367 and slip rate), which are strongly heterogeneous ahead of the rupture front, and more
 368 uniform within the rupture itself. Together with a velocity-cutoff model, this varying crack-
 369 tip slip rate can also induce a delayed stress drop on the asperity behind, which causes
 370 back propagation.

371 Observations indicate that only certain areas experience repeated RTRs with simi-
 372 lar directions, and the propagation velocity differs across locations (Sagae et al., 2023).
 373 This points to spatial variations in roughness as a potential reason. Future studies can
 374 use the distributions of RTRs, propagation velocity, and high-energy radiators (asper-
 375 ities) to test this hypothesis. Simulations that include a heterogeneous asperities-in-matrix
 376 fault also produce back propagation (Luo & Liu, 2021; Peng & Rubin, 2018; Nie & Bar-
 377 bot, 2021). The presence of unstable patches embedded in a stable matrix will produce
 378 variations in stress drops when ruptures cross patches with different frictional proper-
 379 ties, perhaps analogous to the “delayed stress drop” we observed here. Although our sim-
 380 ulations are limited to rate-state friction, the mechanism we identified may also apply
 381 to other cases, as long as two conditions are met. The first is the presence of heteroge-
 382 neous fault properties (such as geometry or friction), capable of efficiently modulating
 383 slip rate along the rupture front. The second is a rate-strengthening mechanism, oper-
 384 ating on a sufficiently short time scale to allow for fast restrengthening and subsequent
 385 stress release upon deceleration, so that a back-propagating front can be triggered. Fur-
 386 ther studies are need to verify whether other stabilizing mechanisms, such as fault dil-
 387 atancy (Segall & Rice, 1995), indeed produce similar behavior.

388 Our simulations show a wide range of propagation velocities. Specifically, the prop-
 389 agation velocity of clustering subevents, forward and back-propagating fronts are on the
 390 order of 0.01, 0.1 and 1 m/s, respectively. SSEs generally travel at about 0.1 m/s; how-
 391 ever, certain SSEs in Japan and Mexico demonstrate a slower pace of about 0.01 m/s
 392 (Gao et al., 2012). Back propagation velocities observed in nature are about 1–5 and
 393 7 – 40 m/s for rapid tremor reversals and along-dip streaks, respectively (Houston et
 394 al., 2011; Shelly et al., 2007; Ghosh et al., 2010). While our simulations accurately cap-
 395 ture the speeds of forward propagation, they seem to underestimate the back-propagating
 396 ones. This implies that the friction parameters in nature are different from those used
 397 in our model or that another unknown mechanism controls this process. We will address
 398 this problem by exploring a broader region of parameter space and developing theoret-
 399 ical formulas in future studies.

400 In addition to back-propagating fronts, fractal faults exhibit sustained, large-scale
 401 re-ruptures. We have identified a mechanism for this behavior, caused by the more ir-
 402 regular roughness distribution on a fractal fault compared to the sinusoidal case, which
 403 can induce pulse-to-crack transitions. Furthermore, natural faults are more complex as
 404 the roughness varies spatially on the same surface indicated by the 3D seismic reflection
 405 (Kirkpatrick et al., 2020) and Lidar observation (Candela et al., 2009). It is easier to in-
 406 duce re-rupture due to the transition from pulse to crack when SSEs propagate from high
 407 roughness to low roughness region. Sagae et al. (2023) shows that the occurrence of sec-

408 ondry tremor migrations depends on the directions of the primary rupture front. Our
 409 mechanism is among the few that offer an explanation for this observation. The pulse-
 410 to-crack transition mediated by roughness is not specific to slow slip, and it may be ap-
 411 plied to a recently observed “boomerang earthquake”, which propagates back through
 412 the initial rupture area (Hicks et al., 2020; S. Yamashita et al., 2022).

413 5 Conclusion

414 We find clustering of slow slip events, different rupture lengths, and varying prop-
 415 agation velocities on a rough fault in the simulations. SSEs tend to arrest and propa-
 416 gate intermittently, which generates a pulse-like slip profile when roughness is high, and
 417 the amplitude of the normal stress perturbation is large. The secondary back propaga-
 418 tion can be induced by fault restrengthening followed by a delayed stress drop when the
 419 rupture passes a low normal stress region. Finally, we find that the transition from pulse
 420 to crack can lead to a large scale re-rupture and back propagation when SSEs propagate
 421 from high to low roughness regions on a fractal fault.

422 Acknowledgments

423 The authors thank Jared Bryan, Xin Cui, William Frank, Zhi Li, Enrico Milanese, and
 424 Qing-Yu Wang for helpful discussions. Y.S. received fundings from MIT EAPS Robert
 425 R Shrock Fellowship, Sven Treitel (1953) Fellowship, and MIT Mathworks Fellowship.

426 Appendix A Estimating propagation velocities

427 To calculate propagation velocity, we used two methods: one for a single event, and
 428 one for clusters of several events. The first method is to use a slip rate threshold to out-
 429 line events and fit the rupture fronts linearly to calculate updip and downdip propaga-
 430 tion velocity (e.g. full rupture in Figure 5b). We can also increase the threshold to de-
 431 lineate the back-propagating fronts and calculate their velocities. We may not capture
 432 all the back-propagating fronts using one threshold, so we use several thresholds and choose
 433 the most representative velocity by visual inspection.

434 Figure 2f also shows clusters of intermittent events that produce a “fish-scale” pat-
 435 tern with each event arresting on a high normal-stress patch. To estimate the propaga-
 436 tion velocity of these clusters, we first outline the subevents by a threshold near the cut-
 437 off velocity (1×10^{-6} m/s). Then we identify clusters as groups of subevents with the
 438 interevent time less than 3 days, which separates the two peaks of the bimodal inter-event
 439 time distribution in Figure 4b. Finally, we use the uppermost/lowermost end of every
 440 event to calculate the updip/downdip propagation velocity of the cluster (e.g. pre-slips
 441 in Figure 5b and subsequent events in Figure 5d).

442 Appendix B Criterion for rupture propagation and arrest

443 In Figure 2, ruptures show pulse-like behavior and stop in high- σ region because
 444 the local toughness there is higher. Here we present a fracture mechanics analysis to ex-
 445 plain rupture propagation and arrest under heterogeneous normal stress. For simplic-
 446 ity, we neglect rupture arrest caused by gradients in the background stress field due to
 447 loading from deep creep (Cattania, 2019). SSEs are mostly nucleated at peaks of nor-
 448 mal stress, so we consider a crack extending from the normal stress maximum at $x =$
 449 0 (eq. 5) to the crack tip at $x = l$ to obtain stress intensity factor K (Tada et al., 1973)
 450 as a function of the stress drop $\Delta\tau$:

$$K = \int_0^l \frac{\sqrt{2}}{\sqrt{\pi(l-x)}} \Delta\tau(x) dx = 2\sqrt{\frac{2l}{\pi}} \Delta\tau_0 + \sqrt{\frac{2\lambda}{\pi}} \Delta\tau_A \left[C(2\sqrt{\frac{l}{\lambda}}) \cos \frac{2\pi l}{\lambda} + S(2\sqrt{\frac{l}{\lambda}}) \sin \frac{2\pi l}{\lambda} \right],$$

$$S(x) = \int_0^x \sin \frac{\pi t^2}{2} dt,$$

$$C(x) = \int_0^x \cos \frac{\pi t^2}{2} dt, \quad (\text{B1})$$

451 where $S(x)$ and $C(x)$ are Fresnel integrals. In Equation B1, $\Delta\tau$ is assumed proportional
 452 to normal stress (Equation 5), with $\Delta\tau_0$ and $\Delta\tau_A$ due to the constant and sinusoidal terms
 453 respectively. The stress drop equals the difference between the initial and minimum fric-
 454 tional stress as:

$$\Delta\tau_{0,A} = \sigma_{0,A} \left(-a \ln \frac{v_{\tau-min}}{v_i} + b \ln \frac{v_c \theta_i / D_c + 1}{v_c / v_{\tau-min} + 1} \right), \quad (\text{B2})$$

455 where v_i and θ_i are the initial slip rate and initial state variable, respectively. In sim-
 456 ulations, the slip rate is $v_i \approx v_{pl}$ in the nucleation zone and it is near steady state as
 457 $v_i \theta_i / D_c = 1$.

458 The local toughness K_c is calculated from the fracture energy G_c as $G_c = \frac{K_c^2}{2G'} =$
 459 $\frac{D_c}{2b\sigma} (\Delta\tau_{p-r})^2$, where $\Delta\tau_{p-r}$ is the peak to residual stress drop. Hawthorne and Rubin (2013a)
 460 derived the stress drop for the velocity-cutoff model as

$$\Delta\tau_{p-r} = b\sigma \left[\ln \left(\frac{v_c \theta_i / 2}{D_c} + 1 \right) - \ln \left(\frac{v_c}{v_{max}/2} + 1 \right) \right]. \quad (\text{B3})$$

461 Thus, K_c is given by

$$K_c = \sqrt{G' b \sigma D_c} \left[\ln \left(\frac{v_c \theta_i / 2}{D_c} + 1 \right) - \ln \left(\frac{v_c}{v_{max}/2} + 1 \right) \right]. \quad (\text{B4})$$

462 To simplify, we use $\theta_i = D_c / v_{pl}$, which represents the creeping region, for K_c all along
 463 the fault. This choice is made because K and K_c have a phase difference of about $\pi/2$,
 464 with the second zero crossing frequently occurring within the creeping region (Figure 3).
 465 Additionally, both the high and low- σ regions undergo creeping following the first rup-
 466 ture.

467 Open Research Section

468 We use MATLAB to plot figures. The results of our simulations (Figure 2, 5 and
 469 7) and simulated SSE catalogs (Figure 4) are archived in Zenodo (Sun & Cattania, 2024).

References

470

- 471 Ampuero, J.-P., & Rubin, A. M. (2008). Earthquake nucleation on rate and state
472 faults—aging and slip laws. *Journal of Geophysical Research: Solid Earth*,
473 *113*(B1).
- 474 Audet, P., & Kim, Y. (2016). Teleseismic constraints on the geological environ-
475 ment of deep episodic slow earthquakes in subduction zone forearcs: A review.
476 *Tectonophysics*, *670*, 1–15.
- 477 Bartlow, N. M., Miyazaki, S., Bradley, A. M., & Segall, P. (2011). Space-time corre-
478 lation of slip and tremor during the 2009 cascadia slow slip event. *Geophysical*
479 *Research Letters*, *38*(18).
- 480 Behr, W. M., & Bürgmann, R. (2021). What’s down there? the structures, materi-
481 als and environment of deep-seated slow slip and tremor. *Philosophical Trans-*
482 *actions of the Royal Society A*, *379*(2193), 20200218.
- 483 Behr, W. M., Gerya, T. V., Cannizzaro, C., & Blass, R. (2021). Transient slow slip
484 characteristics of frictional-viscous subduction megathrust shear zones. *AGU*
485 *Advances*, *2*(3), e2021AV000416.
- 486 Bletery, Q., & Nocquet, J.-M. (2020). Slip bursts during coalescence of slow slip
487 events in cascadia. *Nature communications*, *11*(1), 1–6.
- 488 Bletery, Q., Thomas, A. M., Hawthorne, J. C., Skarbek, R. M., Rempel, A. W., &
489 Krogstad, R. D. (2017). Characteristics of secondary slip fronts associated
490 with slow earthquakes in cascadia. *Earth and Planetary Science Letters*, *463*,
491 212–220.
- 492 Brodsky, E. E., Kirkpatrick, J. D., & Candela, T. (2016). Constraints from fault
493 roughness on the scale-dependent strength of rocks. *Geology*, *44*(1), 19–22.
- 494 Candela, T., Renard, F., Bouchon, M., Brouste, A., Marsan, D., Schmittbuhl, J.,
495 & Voisin, C. (2009). Characterization of fault roughness at various scales:
496 Implications of three-dimensional high resolution topography measurements. In
497 *Mechanics, structure and evolution of fault zones* (pp. 1817–1851). Springer.
- 498 Candela, T., Renard, F., Klinger, Y., Mair, K., Schmittbuhl, J., & Brodsky, E. E.
499 (2012). Roughness of fault surfaces over nine decades of length scales. *Journal*
500 *of Geophysical Research: Solid Earth*, *117*(B8).
- 501 Cattania, C. (2019). Complex earthquake sequences on simple faults. *Geophysical*
502 *Research Letters*, *46*(17-18), 10384–10393.
- 503 Cattania, C., & Segall, P. (2021). Precursory slow slip and foreshocks on rough
504 faults. *Journal of Geophysical Research: Solid Earth*, *126*(4), e2020JB020430.
- 505 Cruz-Atienza, V. M., Villafuerte, C., & Bhat, H. S. (2018). Rapid tremor migration
506 and pore-pressure waves in subduction zones. *Nature communications*, *9*(1), 1–
507 13.
- 508 Erickson, B. A., Jiang, J., Lambert, V., Barbot, S. D., Abdelmeguid, M., Almquist,
509 M., ... others (2023). Incorporating full elastodynamic effects and dipping
510 fault geometries in community code verification exercises for simulations of
511 earthquake sequences and aseismic slip (seas). *Bulletin of the Seismological*
512 *Society of America*, *113*(2), 499–523.
- 513 Eshelby, J. D. (1957). The determination of the elastic field of an ellipsoidal inclu-
514 sion, and related problems. *Proceedings of the royal society of London. Series*
515 *A. Mathematical and physical sciences*, *241*(1226), 376–396.
- 516 Fang, Z., & Dunham, E. M. (2013). Additional shear resistance from fault rough-
517 ness and stress levels on geometrically complex faults. *Journal of Geophysical*
518 *Research: Solid Earth*, *118*(7), 3642–3654.
- 519 Frank, W. B. (2016). Slow slip hidden in the noise: The intermittence of tectonic re-
520 lease. *Geophysical Research Letters*, *43*(19), 10–125.
- 521 Frank, W. B., Rousset, B., Lasserre, C., & Campillo, M. (2018). Revealing the clus-
522 ter of slow transients behind a large slow slip event. *Science advances*, *4*(5),
523 eaat0661.

- 524 Gao, H., Schmidt, D. A., & Weldon, R. J. (2012). Scaling relationships of source pa-
 525 rameters for slow slip events. *Bulletin of the Seismological Society of America*,
 526 *102*(1), 352–360.
- 527 Ghosh, A., Vidale, J. E., Sweet, J. R., Creager, K. C., Wech, A. G., Houston, H.,
 528 & Brodsky, E. E. (2010). Rapid, continuous streaking of tremor in cascadia.
 529 *Geochemistry, Geophysics, Geosystems*, *11*(12).
- 530 Griffith, A. A. (1921). Vi. the phenomena of rupture and flow in solids. *Philosophi-
 531 cal transactions of the royal society of london. Series A, containing papers of a
 532 mathematical or physical character*, *221*(582-593), 163–198.
- 533 Hawthorne, & Bartlow, N. (2018). Observing and modeling the spectrum of a slow
 534 slip event. *Journal of Geophysical Research: Solid Earth*, *123*(5), 4243–4265.
- 535 Hawthorne, Bostock, M. G., Royer, A. A., & Thomas, A. M. (2016). Variations in
 536 slow slip moment rate associated with rapid tremor reversals in c ascadia. *Geo-
 537 chemistry, Geophysics, Geosystems*, *17*(12), 4899–4919.
- 538 Hawthorne, & Rubin, A. (2013a). Laterally propagating slow slip events in a rate
 539 and state friction model with a velocity-weakening to velocity-strengthening
 540 transition. *Journal of Geophysical Research: Solid Earth*, *118*(7), 3785–3808.
- 541 Hawthorne, & Rubin, A. M. (2013b). Tidal modulation and back-propagating
 542 fronts in slow slip events simulated with a velocity-weakening to velocity-
 543 strengthening friction law. *Journal of Geophysical Research: Solid Earth*,
 544 *118*(3), 1216–1239.
- 545 Heimisson, E. R. (2020). Crack to pulse transition and magnitude statistics dur-
 546 ing earthquake cycles on a self-similar rough fault. *Earth and Planetary Sci-
 547 ence Letters*, *537*, 116202.
- 548 Hicks, S. P., Okuwaki, R., Steinberg, A., Rychert, C. A., Harmon, N., Abercrombie,
 549 R. E., ... others (2020). Back-propagating supershear rupture in the 2016 mw
 550 7.1 romanche transform fault earthquake. *Nature Geoscience*, *13*(9), 647–653.
- 551 Houston, H., Delbridge, B. G., Wech, A. G., & Creager, K. C. (2011). Rapid tremor
 552 reversals in cascadia generated by a weakened plate interface. *Nature Geo-
 553 science*, *4*(6), 404–409.
- 554 Idini, B., & Ampuero, J.-P. (2020). Fault-zone damage promotes pulse-like rupture
 555 and back-propagating fronts via quasi-static effects. *Geophysical Research Let-
 556 ters*, *47*(23), e2020GL090736.
- 557 Ikari, M. J., & Saffer, D. M. (2011). Comparison of frictional strength and velocity
 558 dependence between fault zones in the nankai accretionary complex. *Geochem-
 559 istry, Geophysics, Geosystems*, *12*(4).
- 560 Im, K., Saffer, D., Marone, C., & Avouac, J.-P. (2020). Slip-rate-dependent friction
 561 as a universal mechanism for slow slip events. *Nature Geoscience*, *13*(10), 705–
 562 710.
- 563 Irwin, G. R. (1957). Analysis of stresses and strains near the end of a crack travers-
 564 ing a plate.
- 565 Jolivet, R., Candela, T., Lasserre, C., Renard, F., Klinger, Y., & Doin, M.-P. (2015).
 566 The burst-like behavior of aseismic slip on a rough fault: The creeping section
 567 of the haiyuan fault, china. *Bulletin of the Seismological Society of America*,
 568 *105*(1), 480–488.
- 569 Jolivet, R., & Frank, W. (2020). The transient and intermittent nature of slow slip.
 570 *AGU Advances*, *1*(1), e2019AV000126.
- 571 Kirkpatrick, J. D., Edwards, J. H., Verdecchia, A., Kluesner, J. W., Harrington,
 572 R. M., & Silver, E. A. (2020). Subduction megathrust heterogeneity character-
 573 ized from 3d seismic data. *Nature Geoscience*, *13*(5), 369–374.
- 574 Kirkpatrick, J. D., Fagereng, Å., & Shelly, D. R. (2021). Geological constraints on
 575 the mechanisms of slow earthquakes. *Nature Reviews Earth & Environment*,
 576 *2*(4), 285–301.
- 577 Lavier, L. L., Bennett, R. A., & Duddu, R. (2013). Creep events at the brittle duc-
 578 tile transition. *Geochemistry, Geophysics, Geosystems*, *14*(9), 3334–3351.

- 579 Lay, T., Kanamori, H., Ammon, C. J., Koper, K. D., Hutko, A. R., Ye, L., ... Rush-
580 ing, T. M. (2012). Depth-varying rupture properties of subduction zone
581 megathrust faults. *Journal of Geophysical Research: Solid Earth*, *117*(B4).
- 582 Liu, Y., & Rice, J. R. (2005). Aseismic slip transients emerge spontaneously in
583 three-dimensional rate and state modeling of subduction earthquake sequences.
584 *Journal of Geophysical Research: Solid Earth*, *110*(B8).
- 585 Liu, Y., & Rice, J. R. (2007). Spontaneous and triggered aseismic deformation
586 transients in a subduction fault model. *Journal of Geophysical Research: Solid
587 Earth*, *112*(B9).
- 588 Luo, Y., & Ampuero, J.-P. (2018). Stability of faults with heterogeneous friction
589 properties and effective normal stress. *Tectonophysics*, *733*, 257–272.
- 590 Luo, Y., & Liu, Z. (2021). Fault zone heterogeneities explain depth-dependent pat-
591 tern and evolution of slow earthquakes in cascadia. *Nature communications*,
592 *12*(1), 1–13.
- 593 Marone, C. (1998). Laboratory-derived friction laws and their application to seismic
594 faulting. *Annual Review of Earth and Planetary Sciences*, *26*(1), 643–696.
- 595 Michel, S., Gualandi, A., & Avouac, J.-P. (2019). Similar scaling laws for earth-
596 quakes and cascadia slow-slip events. *Nature*, *574*(7779), 522–526.
- 597 Nie, S., & Barbot, S. (2021). Seismogenic and tremorgenic slow slip near the sta-
598 bility transition of frictional sliding. *Earth and Planetary Science Letters*, *569*,
599 117037.
- 600 Obara, K., Hirose, H., Yamamizu, F., & Kasahara, K. (2004). Episodic slow slip
601 events accompanied by non-volcanic tremors in southwest japan subduction
602 zone. *Geophysical Research Letters*, *31*(23).
- 603 Obara, K., Matsuzawa, T., Tanaka, S., & Maeda, T. (2012). Depth-dependent mode
604 of tremor migration beneath kii peninsula, nankai subduction zone. *Geophys-
605 ical Research Letters*, *39*(10).
- 606 Peng, & Gombert, J. (2010). An integrated perspective of the continuum between
607 earthquakes and slow-slip phenomena. *Nature geoscience*, *3*(9), 599–607.
- 608 Peng, & Rubin, A. M. (2018). Simulating short-term evolution of slow slip influ-
609 enced by fault heterogeneities and tides. *Geophysical Research Letters*, *45*(19),
610 10–269.
- 611 Power, W., Tullis, T., Brown, S., Boitnott, G., & Scholz, C. (1987). Roughness of
612 natural fault surfaces. *Geophysical Research Letters*, *14*(1), 29–32.
- 613 Power, W. L., & Tullis, T. E. (1991). Euclidean and fractal models for the descrip-
614 tion of rock surface roughness. *Journal of Geophysical Research: Solid Earth*,
615 *96*(B1), 415–424.
- 616 Radiguet, M., Cotton, F., Vergnolle, M., Campillo, M., Valette, B., Kostoglodov, V.,
617 & Cotte, N. (2011). Spatial and temporal evolution of a long term slow slip
618 event: the 2006 guerrero slow slip event. *Geophysical Journal International*,
619 *184*(2), 816–828.
- 620 Renard, F., & Candela, T. (2017). Scaling of fault roughness and implications for
621 earthquake mechanics. *Fault zone dynamic processes: Evolution of fault proper-
622 ties during seismic rupture*, *227*, 197–216.
- 623 Rice, J. R. (1993). Spatio-temporal complexity of slip on a fault. *Journal of Geo-
624 physical Research: Solid Earth*, *98*(B6), 9885–9907.
- 625 Rogers, G., & Dragert, H. (2003). Episodic tremor and slip on the cascadia subduc-
626 tion zone: The chatter of silent slip. *Science*, *300*(5627), 1942–1943.
- 627 Romanet, P., Sato, D. S., & Ando, R. (2020). Curvature, a mechanical link between
628 the geometrical complexities of a fault: application to bends, kinks and rough
629 faults. *Geophysical Journal International*, *223*(1), 211–232.
- 630 Rousset, B., Fu, Y., Bartlow, N., & Bürgmann, R. (2019). Weeks-long and years-
631 long slow slip and tectonic tremor episodes on the south central alaska megath-
632 rust. *Journal of Geophysical Research: Solid Earth*, *124*(12), 13392–13403.

- 633 Rubin, A. M. (2008). Episodic slow slip events and rate-and-state friction. *Journal*
634 *of Geophysical Research: Solid Earth*, *113*(B11).
- 635 Rubin, A. M., & Ampuero, J.-P. (2005). Earthquake nucleation on (aging) rate and
636 state faults. *Journal of Geophysical Research: Solid Earth*, *110*(B11).
- 637 Ruina, A. (1983). Slip instability and state variable friction laws. *Journal of Geo-*
638 *physical Research: Solid Earth*, *88*(B12), 10359–10370.
- 639 Saffer, D. M., Frye, K. M., Marone, C., & Mair, K. (2001). Laboratory results indic-
640 ating complex and potentially unstable frictional behavior of smectite clay.
641 *Geophysical Research Letters*, *28*(12), 2297–2300.
- 642 Sagae, K., Nakahara, H., Nishimura, T., & Imanishi, K. (2023). Fine structure of
643 tremor migrations beneath the kii peninsula, southwest japan, extracted with
644 a space-time hough transform. *Journal of Geophysical Research: Solid Earth*,
645 *128*(6), e2022JB026248.
- 646 Segall, P., & Bradley, A. M. (2012). Slow-slip evolves into megathrust earthquakes in
647 2d numerical simulations. *Geophysical Research Letters*, *39*(18).
- 648 Segall, P., & Rice, J. R. (1995). Dilatancy, compaction, and slip instability of a
649 fluid-infiltrated fault. *Journal of Geophysical Research: Solid Earth*, *100*(B11),
650 22155–22171.
- 651 Segall, P., Rubin, A. M., Bradley, A. M., & Rice, J. R. (2010). Dilatant strengthen-
652 ing as a mechanism for slow slip events. *Journal of Geophysical Research: Solid*
653 *Earth*, *115*(B12).
- 654 Shelly, D. R., Beroza, G. C., & Ide, S. (2007). Complex evolution of transient slip
655 derived from precise tremor locations in western shikoku, japan. *Geochemistry,*
656 *Geophysics, Geosystems*, *8*(10).
- 657 Sun, Y., & Cattania, C. (2024, April). *Simulation Results in the Paper "Propaga-*
658 *tion of Slow Slip Events on Rough Faults: Clustering, Back Propagation, and*
659 *Re-rupturing" [Dataset]*. Zenodo. Retrieved from [https://doi.org/10.5281/](https://doi.org/10.5281/zenodo.10988744)
660 [zenodo.10988744](https://doi.org/10.5281/zenodo.10988744) doi: 10.5281/zenodo.10988744
- 661 Tada, H., Paris, P. C., & Irwin, G. R. (1973). The stress analysis of cracks. *Hand-*
662 *book, Del Research Corporation*, *34*.
- 663 Wallace, L. M. (2020). Slow slip events in new zealand. *Annual Review of Earth and*
664 *Planetary Sciences*, *48*, 175–203.
- 665 Wech, A. G., & Bartlow, N. M. (2014). Slip rate and tremor genesis in cascadia.
666 *Geophysical Research Letters*, *41*(2), 392–398.
- 667 Yamashita, Yakiwara, H., Asano, Y., Shimizu, H., Uchida, K., Hirano, S., ... others
668 (2015). Migrating tremor off southern kyushu as evidence for slow slip of a
669 shallow subduction interface. *Science*, *348*(6235), 676–679.
- 670 Yamashita, S., Yagi, Y., & Okuwaki, R. (2022). Irregular rupture propagation
671 and geometric fault complexities during the 2010 mw 7.2 el mayor-cucapah
672 earthquake. *Scientific reports*, *12*(1), 1–10.
- 673 Yin, A. (2018). Water hammers tremors during plate convergence. *Geology*, *46*(12),
674 1031–1034.
- 675 Yin, A., Xie, Z., & Meng, L. (2018). A viscoplastic shear-zone model for deep (15–50
676 km) slow-slip events at plate convergent margins. *Earth and Planetary Science*
677 *Letters*, *491*, 81–94.